NASA-CR-195877

FINAL REPORT

PLASMA AND RADIO WAVES FROM NEPTUNE: SOURCE MECHANISMS AND PROPAGATION

For the Period:

1 January 1991 through 31 March 1994

SwRI Project 15-4167

NASA Grant No. NAGW-2412

Prepared by

H.K. Wong

for

National Aeronautics and Space Administration
Solar System Exploration Division
Neptune Data Analysis Program
Washington, DC 20546

(NASA-CR-195877) PLASMA AND RADIO WAVES FROM NEPTUNE: SOURCE MECHANISMS AND PROPAGATION Final Report, 1 Jan. 1991 - 31 Mar. 1994 (Southwest Research Inst.) 34 p

N94-33103

Unclas

G3/91 0008627

I. INTRODUCTION

This report summarizes results obtained through the support of NASA Grant NAGW-2412. The objective of this project is to conduct a comprehensive investigation of the radio wave emission observed by the Planetary Radio Astronomy (PRA) instrument on board Voyager 2 as if flew by Neptune. This study has included data analysis, theoretical and numerical calculations, ray tracing, and modeling to determine the possible source mechanism(s) and locations of the Neptune radio emissions. We have completed four papers, which are included in the appendix. The paper "Modeling of whistler ray paths in the magnetosphere of Neptune" investigated the propagation and dispersion of lighting-generated whistler in the magnetosphere of Neptune by using three dimensional ray tracing. The two papers "Numerical simulations of bursty radio emissions from planetary magnetospheres" and "Numerical simulations of bursty planetary radio emissions" employed numerical simulations to investigate an alternate source mechanism of bursty radio emissions in addition to the cyclotron maser instability. We have also studied the possible generation of Z and whistler mode waves by the temperature anisotropic beam instability and the result was published in "Electron cyclotron wave generation by relativistic electrons".

Besides the aforementioned studies, we have also collaborated with Drs. Sawyer, King, Romig, and Warwick of the PRA team to investigate various aspects of the radio wave data. Two papers have been submitted for publication and the abstracts of these papers are also listed in the appendix.

In the next section we summarize the research results.

II. SUMMARY OF RESEARCH RESULTS

A. Modeling of Whistler Ray Paths in the Magnetosphere of Neptune

During the Voyager 2 flyby of Neptune, 16 "whistlerlike" events near the magnetic equator were observed. Using a simple empirical plasma model based on observational constraints and an offset titled dipole magnetic field model, a three dimensional ray tracing study is performed to investigate the propagation and dispersion of lightning-generated whistlers in the magnetospheres of Neptune. Source positions for the whistlers are chosen along magnetic field lines with $L < 3$ in agreement with observations. Whistlers with frequencies of about 10 kHz generally propagate very nearly the resonance cone angle for most of the ray path, which produces dispersions considerably larger than those predicted for quasiparallel propagation. In general, the whistlers were found to propagate about 10 degree in magnetic longitude during one hop and to cross L shells. These results strongly support the existence of whistlers at Neptune. The large dispersions are attributed to the large cold plasma population at Neptune, which leads to propagation very near the resonance cone angle for a large part of the ray path.

B. Numerical Simulations of Bursty Radio Emissions from Planetary Magnetospheres

The Voyager 2 spacecraft has observed both smooth and bursty radio emissions from Uranus and Neptune. These emissions are known to be freely propagating primarily in the right-hand circularly polarized (RCP) mode with the bursty emissions having duration periods as short as a few tenths of a second and the smooth emissions being observed over periods of a few hours. While the smooth emission is probably due to the cyclotron maser instability, some other processes might be responsible for the generation of the bursty emissions. It is proposed that one important difference in mechanisms is that the smooth emissions are associated with continuous injection of electrons while the bursty emissions are associated with impulsive injection. In the latter case, the electron distribution can develop a beam feature with a temperature anisotropy. It is shown via one-dimensional (three velocity) relativistic particle simulations that while the beam may be initially unstable to an electrostatic instability, this instability quickly saturates and eventually the beam is unstable to a strong electromagnetic beam instability which utilizes the temperature anisotropy as free energy; a beam feature is not explicitly needed for the growth of this electromagnetic instability. The radiation generated by the instability is able to convert particle energy to wave energy at similar levels at the maser instability. It is also postulated that some of the radiation generated below the local X mode cutoff may also be able to escape and be detected remotely via mode conversion between regions where field-aligned currents produce local perturbations in the magnetic field.

C. Electron Cyclotron Wave Generation by Relativistic Electrons

Besides the freely propagating extraordinary (X) and ordinary (O) mode waves, Z mode waves with frequencies below the electron cyclotron frequency have also been observed in planetary magnetospheres. It is shown that an energetic electron distribution which has a temperature anisotropy, or which is gyrating about a DC magnetic field, can generate electron cyclotron waves with frequencies below the electron cyclotron frequency. Relativistic effects are included in the stability analysis and are shown to be quantitatively important. The basic idea of the mechanism is the coupling of the beam mode to slow waves. The unstable electron cyclotron waves are predominately electromagnetic and right-hand polarized. For a low density plasma in which the electron plasma frequency is less than the electron cyclotron frequency, the excited waves can have frequencies above or below the electron plasma frequency. This instability might account for observed Z mode waves in the magnetosphere of Neptune.

III. LIST OF PUBLICATIONS

1. Menietti, J. D., D. Tsintikidis, D. A. Gurnett, and D. B. Curran, Modeling of Whistler Ray Paths in the Magnetosphere of Neptune, *J. Geophys. Res.*, **96**, 19117, 1991.

2. Winglee, R. M., J. D. Menietti, and H. K. Wong, Numerical Simulations of Bursty Radio Emissions from Planetary Magnetospheres, *J. Geophys. Res.*, **97**, 17131, 1992.

3. Winglee, R. M., J. D. Menietti, and H. K. Wong, Numerical Simulations of Bursty Planetary Radio Emissions, in Planetary Radio Emissions III, ed. by H. O. Rucker, S. J. Bauer, and M. L. Kaiser, Osterreichischen Akademie Der Wissenschaften, Wien, Austria, p. 317, 1992.

4. Wong, H. K., and M. L. Goldstein, Electron Cyclotron Wave Generation by Relativistic Electrons, *J. Geophys. Res.*, **99**, 235, 1994.

APPENDIX

JOURNAL OF GEOPHYSICAL RESEARCH, VOL. 96, SUPPLEMENT, PAGES 19,117–19,122, OCTOBER 30, 1991

Modeling of Whistler Ray Paths in the Magnetosphere of Neptune

J. D. MENIETTI

Space Sciences Department, Southwest Research Institute, San Antonio, Texas

D. TSINTIKIDIS AND D. A. GURNETT

Department of Physics and Astronomy, University of Iowa, Iowa City

D. B. CURRAN

Space Sciences Department, Southwest Research Institute, San Antonio, Texas

A three-dimensional ray tracing program is used to investigate the propagation and dispersion of lightning-generated whistlers in the magnetosphere of Neptune. A simple empirical magnetospheric plasma model based on observational constraints is used for the plasma density distribution, and an offset tilted dipole model is used for the magnetic field. Source positions for the whistlers are chosen along magnetic field lines with $L < 3$ in agreement with observations. Whistlers with frequencies of about 10 kHz generally propagate very near the resonance cone angle for most of the ray path, which produces dispersions considerably larger than those predicted for quasiparallel propagation. Dispersions computed using our "standard" plasma density model are over 30,000 s $\sqrt{\text{Hz}}$ for "one-hop" whistlers which is comparable to observed values. In general, the whistlers were found to propagate about 10° in magnetic longitude during one hop and to cross L shells. These results strongly support the existence of whistlers at Neptune. The large dispersions are attributed to the large cold plasma population at Neptune which leads to propagation very near the resonance cone angle for a large part of the ray path.

Introduction

During the Voyager 2 flyby of Neptune, which occurred on August, 25, 1989, the plasma wave instrument detected 16 "whistlerlike" events near the magnetic equator at radial distances ranging from 1.30 to 1.99 R_N [*Gurnett et al.*, 1989, 1990]. The frequency ranged from 6.1 to 12.0 kHz, and the dispersions fit the Eckersley law for lightning-generated whistlers. The existence of whistler mode emissions (which propagate at frequencies less than the minimum of either the gyrofrequency, f_c, or the plasma frequency, f_p) sets a limit on the density at the point of observation. The magnetic field was directly measured at the point of observation, and the local gyrofrequency during the observations was at least 100 kHz. *Belcher et al.* [1989] have reported that plasma density measurements near closest approach (CA) are typically 0.01 to 0.1 cm^{-3} with a maximum of 1.4 cm^{-3} near the magnetic equator. These values are dependent on ion composition which is uncertain. However, the instrument was probably not sensitive to cold plasma because the Faraday cups were not favorably oriented at the time of CA (R. McNutt, private communication, 1990). We also note that *Barbosa et al.* [1990] have estimated the density at this time based on plasma wave measurements of ion cyclotron harmonics to be in the range of 1 to 10 cm^{-3}, again dependent on the ion composition. *Sawyer et al.* [1990] reported what appear to be electron cyclotron harmonics at this time in the Planetary Radio Astronomy data, which may also indicate higher densities based on the cyclotron-maser instability. The topic of plasma density was discussed at great length by *Gurnett et al.* [1990], and led the authors to suggest that the signals were in fact whistlers. Gurnett et al. believe the density at the point of observation must be at least 30 to 100 cm^{-3}.

One result that is difficult to understand is the extremely large dispersions, typically 26,000 s $\sqrt{\text{Hz}}$. The dispersion is defined by the Eckersley law, $t = D/\sqrt{f}$, where t is the travel time, f is the frequency and D is a contant called the dispersion. For low frequencies and propagation parallel to the magnetic field the dispersion constant D is given by

$$D = (1/2c) \int \frac{f_p\,ds}{\sqrt{f_c}}, \tag{1}$$

where ds is elemental distance along the ray path. Based on minimum and maximum estimates of the density in the magnetosphere, Gurnett et al. calculated that path lengths ranging from ~50 to over 2000 R_N are required to achieve the observed dispersion. While whistlers observed at Earth are in rare cases known to have bounced as many as 200 times, it is difficult to imagine an electromagnetic wave surviving such long path lengths without suffering significant damping, scattering, or other processes that would strongly degrade the amplitude.

In this paper we present a preliminary study of whistler propagation based on three-dimensional ray tracing. We emphasize that these are initial results and more work needs to be done to understand the details of the observations. The results show that very large dispersions are obtained even without multiple bounces. The large dispersions are the result of propagation very near the resonance cone angle for a large part of the ray path. Such dispersions are considerably larger than predicted by the Eckersley law, which is not valid at large wave normal angles.

Plasma and Magnetic Field Models

The magnetic field model is an offset tilted dipole which is a refinement (OTD2) of an earlier model developed by Ness et al.

Paper number 91JA01651.
0148-0227/91/91JA-01651$05.00

[1989]. This model is based on a dipole, with magnetic moment of $\mu = 0.13\ GR^3_N$ tilted by about 45° with respect to the rotation axis and is offset from the center by 0.55 R_N. This model is known to be quite accurate along the spacecraft trajectory at distances greater than about 3 R_N, but may have significant deviations from the real field close to the planet (N.F. Ness, private communication, 1990). The large offset produces a strong asymmetry in the field strength between northern and southern magnetic hemispheres, and the tilt produces a strong longitudinal asymmetry. As will be shown, these asymmetries have noticeable effects on whistler propagation.

The plasma model consists of an ionospheric model and a magnetospheric model. The ionospheric model is due to *Shinagawa and Waite* [1989]. Specifically we have used the model represented by curve "a" in their Figure 1, page 946. This was their "standard case" model and produced peak densities of about 6 x 10^4 cm^{-3} at an altitude of about 1700 km. This model differs from the results of the Voyager radio science observations [*Tyler et al.*, 1989]. The maximum density obtained from the radio occultations was about 2.5 x 10^3 cm^{-3} at an altitude of about 1400 km, but it is to be noted that these observations were made near the terminator. Most likely the electron densities are much higher on the dayside of Neptune, particularly near the subsolar point. We used a simple linear fit to the logarithmic function of Shingawa and Waite as follows:

$$n_{ionos} = 10^{mr+n_i}\ (cm^{-3}) \tag{2}$$

with m = -3.16 x 10^{-4}, n_i = 13.18, and r the radial distance in kilometers. For the magnetospheric electron density we have introduced a simple empirical model with a radial dependence only:

$$n = n_o + Ce^{-k(r/R_N-1)^2} \tag{3}$$

with C = 99.91, k = 0.567, n_o = 0.09, and R_N = 24,765 km. The constants were selected to produce a density of about 30 cm^{-3} at L = 3. This value is approximately midrange between the estimate of the density range suggested by *Gurnett et al.* [1990]. For this initial study no local time dependence was incorporated

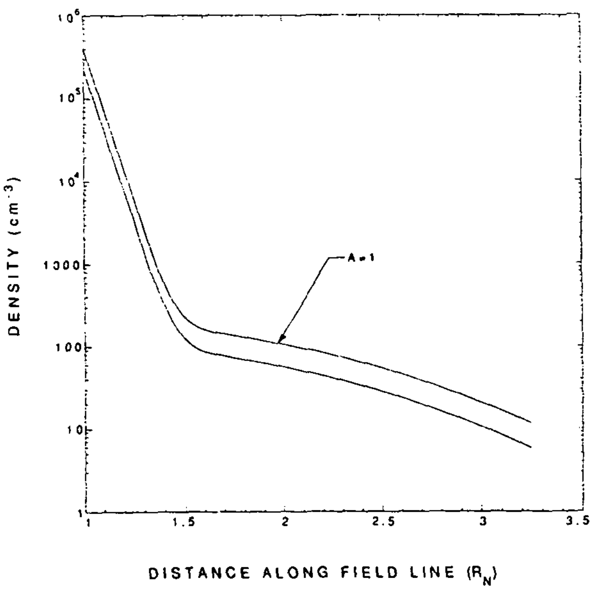

Fig. 1. Density versus distance along a magnetic field line. The footprint of the magnetic field line chosen was λ = 40°, Λ = 140°. The curves are for equation (4) with A = 0 and A = 1.

in the density model. We have also examined a modification of this magnetospheric model by introducing a latitudinal dependence with a peak density at the geographic equator. The specific form of the latitudinal dependence is given by

$$n' = n[1 + A\cos(\lambda)] \tag{4}$$

where n' is the density, A is a variable, and λ is the geographic latitude. A plot of the density versus distance along a sample magnetic field line for both equations (3) and (4) is shown in Figure 1.

RAY TRACING

Ray tracing calculations were performed using the three-dimensional code that has been discussed in the past [cf. *Menietti et al.*, 1990]. This code is based on the cold plasma theory of *Stix* [1962] and *Haselgrove's* [1955] set of first-order differential equations. Early in the study it was discovered, however, that whistler wave propagation near the resonance cone was occurring because of the high ionospheric and magnetospheric densities. When this happens, the index of refraction becomes so large that numerical instabilities prohibit further integration. To circumvent this problem, a modification of the basic equations was introduced on the basis of the scheme of *Cerisier* [1970], also utilized by *Cairo and Lefeuvre* [1986]. The fundamental change was the introduction of the following logarithmic derivative:

$$\frac{d}{ds}\ln(\cos^2\psi - \cos^2\psi_r) = -2\sin\psi\cos\psi\frac{d\psi}{ds} - \frac{d}{ds}\cos^2\psi_r\ /\ (\cos^2\psi - \cos^2\psi_r) \tag{5}$$

with

$$\frac{d}{ds}\cos^2\psi_r = \frac{1}{(S-P)}\frac{dS}{ds} - \frac{S}{(S-P)^2}\left[\frac{dS}{ds} - \frac{dP}{ds}\right]$$

where Ψ is the wave normal angle, s is the ray path, and Ψ_r is the resonance cone angle, which according to *Stix* [1962] is given by

$$\tan^2(\psi_r) = -P/S \tag{6}$$

with P and S defined by *Stix* [1962]. As discussed in detail by *Cerisier* [1970], because of the slow logarithmic dependence, equation (5) allows the evaluation of Ψ and numerical integration near the resonance cone angle.

The Eckersley law dispersion given by equation (1) is only valid for low frequencies and small wave normal angles, such that f/f_c << cos(ψ). This assumption is called the quasi-parallel approximation [*Helliwell*, 1965]. The quasi-parallel approximation fails for propagation near the resonance cone angle, particularly when the ray path is at larger distances (r ~ 2 R_N) from Neptune. As we describe below, we initially calculate the time delay, T, for a large number of rays at f = 10 kHz in order to obtain candidate source positions. To compute T we use the formula $T = \int ds/v_g$ where v_g is the group velocity. We later estimate D by comparing T for a number of ray paths, from the same source point, at different frequencies. The initial wave normal angles are adjusted such that the ray paths for each frequency intersect one point in the magnetosphere.

RESULTS

The whistlers observed by Voyager 2 all occurred within about 35° of the magnetic equator and at 1.4 < L < 2. The L values were obtained from N.F. Ness (personal communication, 1991).

Using the OTD2 model we identified source positions near the surface of Neptune for which $L < 3$. Generally speaking there were two such positions along each longitude meridian of Neptune, one in each hemisphere. Initially we confined our attention to source positions located nearer the north (weaker) magnetic pole because the lower hybrid frequency, f_{LH}, was much lower in this case. This is true because

$$1/f_{LH}^2 = 1/f_{ci}^2 + 1/f_{pi}^2 + 1/(f_{ci} f_c) \quad (7)$$

and is strongly dependent on the local field strength through f_c. In this equation, f_{ci} and f_{pi} are the ion cyclotron frequency and ion plasma frequency, respectively. As an example, for a source near the north magnetic pole ($\lambda = 5°$, $\Lambda = 140°$), $f_{ci} \sim 8.5 \times 10^{-3}$ kHz, $f_{pi} \sim 54$ kHz, $f_c \sim 132$ kHz, and $f_{LH} \sim 3.1$ kHz. In contrast for a source near the much stronger south magnetic pole ($\lambda = -30°$, $\Lambda = 250°$), $f_{ci} \sim 3.1 \times 10^{-2}$ kHz, $f_{pi} \sim 54$ kHz, $f_c \sim 1710$ kHz, and $f_{LH} \sim 32.1$ kHz. When $f < f_{LH}$, the index-of-refraction surface is closed, and reflection occurs when f approaches f_{LH} or if the wave normal angle approaches 90°. A wave propagating away from the surface in a region where $f_{LH} >> f$ (where magnetic field strength is large) can be trapped in the ionosphere, and a wave from the magnetosphere can be reflected back. For $f > f_{LH}$, the index-of-refraction surface changes to an open surface with a discontinuity at the resonance cone angle.

The rays were launched at an altitude of 1700 km, near the peak ionospheric density, at a wave normal angle that corresponded to a wave vector directed radially outward (vertical) from the planet. A vertical initial wave normal direction is used because whistler mode waves from lightning are expected to be refracted to near vertical due to the large index of refraction in the ionosphere. Generally, the initial wave normal angle was about 25° to 30°. The frequency was 10 kHz, and source positions were chosen every 10° of longitude. Source positions with the smallest local magnetic field strength usually produced the largest time delays. This follows approximately from the equation for D which shows that the dispersion is inversely proportional to $\sqrt{f_c}$ (see equation (1)). In Table 1 we list a summary of results for various source positions and for two density models as identified in the last column. The angle β is the azimuthal angle about the magnetic field; i.e., this angle determined the plane in which the ray was launched. The approximate L shell for a particular ray path as it crossed the magnetic equator is designated as L_{avg}. This L value is typically different from the L value of the source point because of deviations of the ray path from a fixed L shell.

The time delays listed in the table are the total integrated values at a point near the magnetic equator before the ray propagates to the opposite hemisphere. Many of the travel times in Table 1 are much larger than comparable values calculated at Earth or at Jupiter. The reason for the large travel times is twofold. First, the enormous dimensions of Neptune produce a ray path much longer than any obtained at Earth, which causes a corresponding increase in the dispersion. Second, the wave normal angles of the rays are very near the resonance cone angle for a large part of the ray path. At Jupiter the magnetospheric densities are apparently much lower than those at Neptune, and the magnetic field strength is much larger. Consequently, the lower hybrid frequency will be larger than the whistler frequency for much of the ray path thereby resulting in an open index-of-refraction surface with no resonance cone.

It is clear from the table that source points near a longitude of 130° produce the largest values of T. For $\beta = 58°$, $\lambda = 25°$, $\Lambda =$ 130° we obtained $T = 61.6$ s. This is about 1/4 of the value of $T \sim 250$ s reported by *Gurnett et al.* [1990]. In Figure 2 we show a three-dimensional plot of the ray path for this last case. Superimposed on the figure is the magnetic field line along which the source was located. The solid circle indicates the south magnetic pole. Clearly the ray path diverges substantially from the magnetic field line and extends to large L values. Two

TABLE 1. Selected Source Positions and Time Delays (f = 10 kHz)

β, deg	Source Position λ, deg	Λ, deg	L_{avg}	T, s	Density Model A
50	-10	70	2.7	11.4	0
49	0	100	2.7	7.6	0
57	18	130	2.8	3.9	0
67	35	150	2.7	3.6	0
174	70	260	2.6	3.8	0
34	10	10	2.4	6.4	1.0
72	-20	30	1.8	1.6	1.0
49	0	100	2.7	15.5	1.0
53	10	120	2.9	9.4	1.0
58	25	130	2.8	61.6	1.0
61	25	140	2.8	35.1	1.0
67	35	150	2.7	23.3	1.0
93	60	180	2.7	4.6	1.0
103	65	190	2.6	4.9	1.0
123	70	210	2.4	8.3	1.0
174	70	260	2.5	12.0	1.0
85	49	330	2.2	6.0	1.0

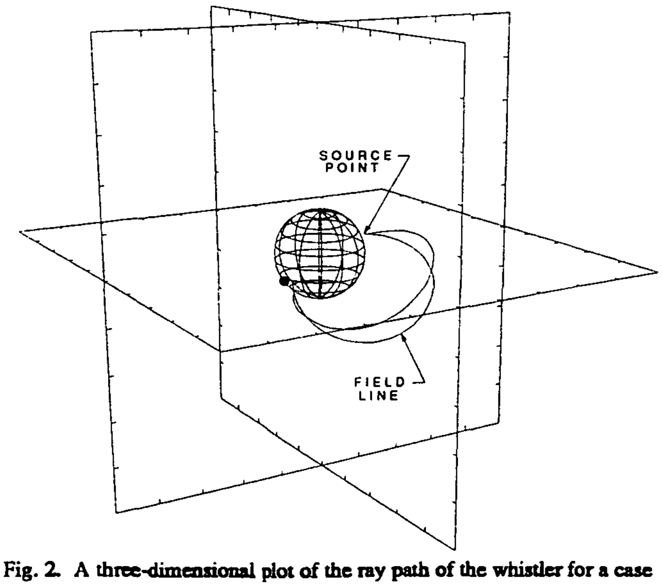

Fig. 2. A three-dimensional plot of the ray path of the whistler for a case where $T \sim 61.6$ s. The field line along which the source point was located is shown as well as the south magnetic pole (black dot).

perspective plots of the ray path in two dimensions are shown in Figure 3. The total change in magnetic longitude is about 10°. In Figure 4 we plot Ψ and Ψ_r versus ray path, s, and in Figure 5 we plot the index of refraction, N, and v_g/c (group velocity/speed of light) versus s. We may use these figures to understand a little more clearly the behavior of the whistlers in the ionosphere and magnetosphere of Neptune.

In Figure 4 we see that the wave normal angle, Ψ, is initially about 23° and that the wave propagates along the density gradient. The resonance cone angle is near 90° at this point. As the wave propagates out of the ionosphere, the wave normal angle initially decreases as the wave leaves the ionosphere, and then increases, rapidly approaching the resonance cone angle. In Figure 5 we see that the index of refraction initially decreases as the wave propagates out of the ionosphere but soon begins to increase rapidly as Ψ approaches Ψ_r. As propagation proceeds into the magnetosphere and both f_p and f_c decrease, Ψ approaches Ψ_r and the magnitude of Ψ gradually increases and then decreases rapidly when Ψ is no longer close to Ψ_r. The wave again begins to approach Neptune and a new field line footprint in the opposite hemisphere. During this time both Ψ and N steadily decrease. As the wave enters the ionosphere for the second time near the conjugate footprint, at the south magnetic pole, Ψ_r increases to ~ 90°, and Ψ begins to increase. Because the south magnetic pole surface field strength is much larger than the north polar field strength, the gyrofrequency becomes relatively quite large, and f_p/f_c becomes less than 1 (Figure 6). The index of refraction reaches a minimum and begins to increase as f_p/f_c begins to increase, once again becoming greater than 1 well inside the ionosphere.

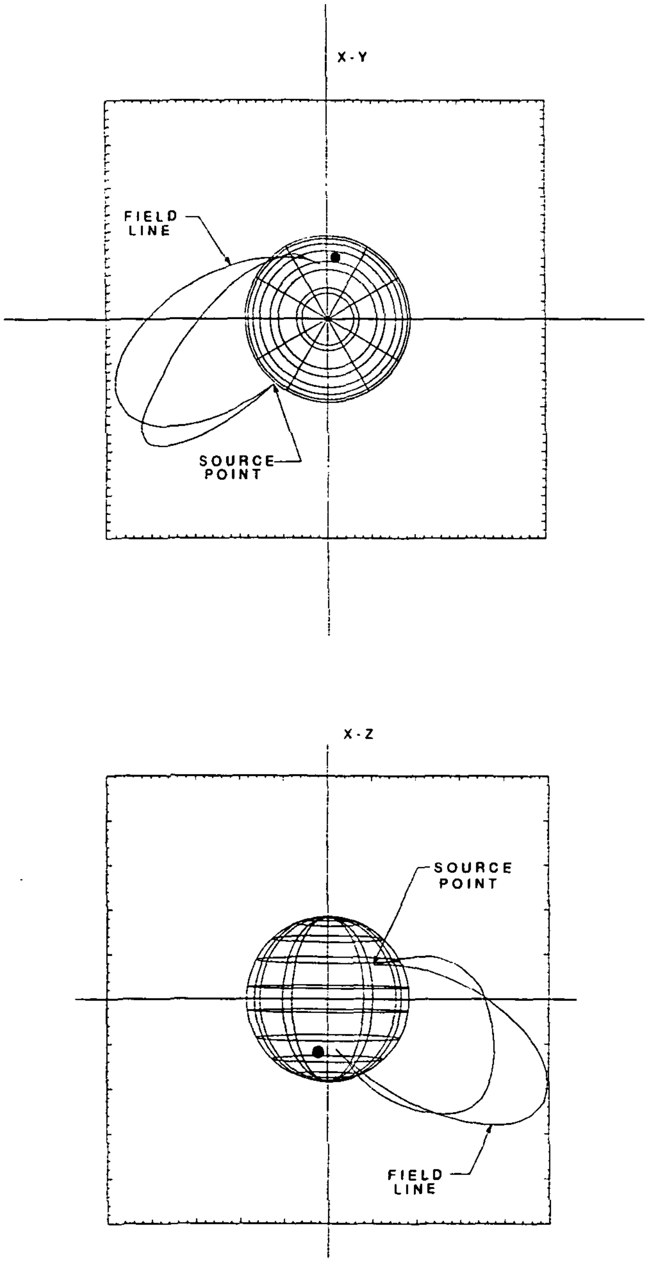

Fig. 3. Two perspectives in two dimensions of the same ray path shown in Figure 2. The top panel is the perspective from the north geographic pole.

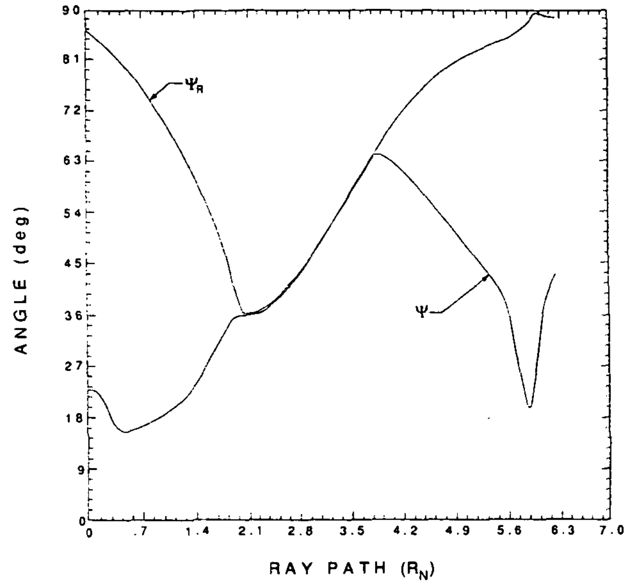

Fig. 4. The wave normal angle, Ψ, and the resonance cone angle, Ψ_r, versus ray path for the case with $T = 61.6$ s.

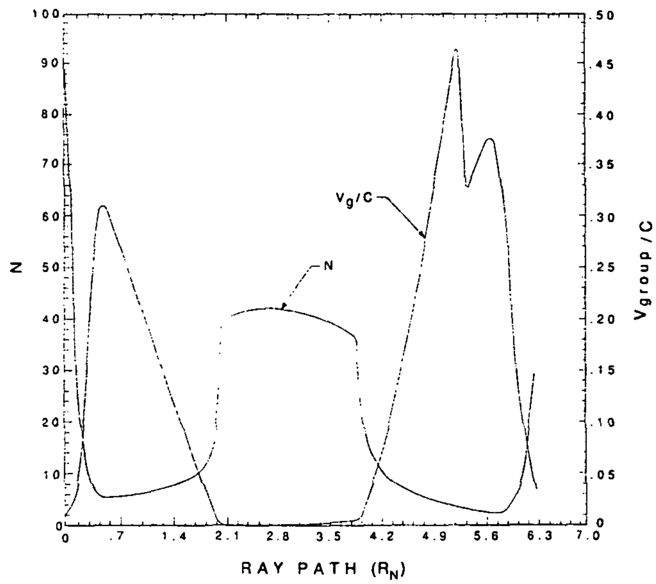

Fig. 5. The index of refraction and v_g/c versus ray path for the case with $T = 61.6$ s.

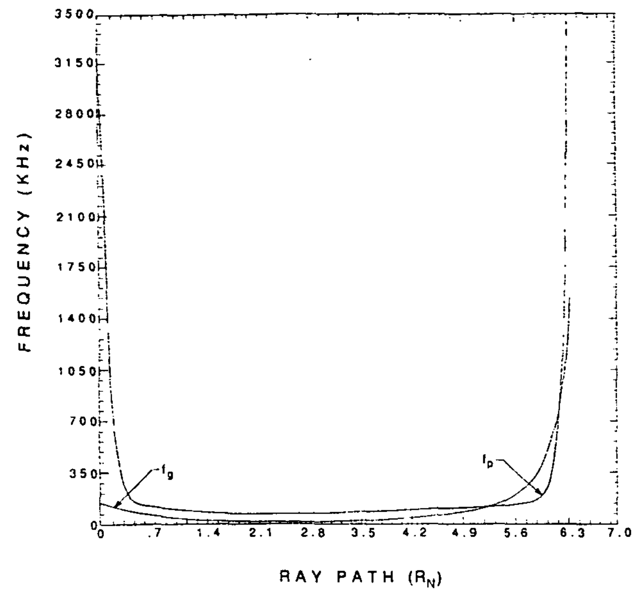

Fig. 6. Gyrofrequency and plasma frequency versus ray path for the case with $T = 61.6$ s.

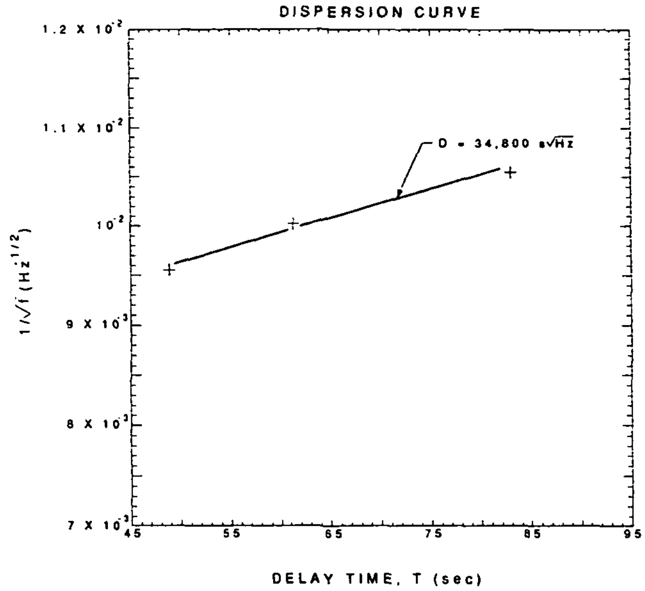

Fig. 7. $1/\sqrt{f}$ versus delay time T for whistlers with a source at $\lambda = 25°$, $\Lambda = 130°$.

CALCULATION OF DISPERSION

In order to estimate the dispersion of the rays we have evaluated the time delay for several frequencies for specific source points. The technique is tedious because, for a fixed source point in the ionosphere we require that the ray for each chosen frequency intercept a given observation point in the magnetopshere. The observation point was selected to be near the magnetic equator at a distance of ~ 2.4 R_N. This point was not an actual spacecraft position, but was chosen to be near sources which produced the largest dispersion. There are at least four parameters that could be adjusted at the source point to accomplish this: Ψ, β, λ, and Λ. In the limited time and finances available for this study, we were able to find ray paths at three frequencies that intercepted at the common point for whistlers with a source point at $\lambda = 25°$, $\Lambda = 130°$. We see from Table 1 that the total time delay for this source point at a frequency of 10 kHz is about 62 s.

To minimize the time required to obtain satisfactory results we limited the variable parameters to Ψ and β. We found interceptions for three frequencies with at most a 1° change in β. The initial value of the wave vector k varied by a maximum of 0.1° from the vertical. We display plots of $1/\sqrt{f}$ versus T in Figure 7. The dispersion for this case is found from a least squares fit to be D ~ 34,800 s $\sqrt{\text{Hz}}$. The latter value is comparable to the value of ~ 26,000 s $\sqrt{\text{Hz}}$ obtained by *Gurnett et al.* [1990] for most of the whistlers. It is important to note that *Gurnett et al.* [1990] obtained D from the observations by measuring the slope of the curve of $1/\sqrt{f}$ versus delay time. Their values are strictly determined by arrival time measurements as a function of frequency and are not dependent on the validity of equation (1). Our calculated values of D are obtained by essentially the same technique that was used to obtain the observed values.

SUMMARY AND DISCUSSION

We have shown that whistler propagation in the magnetosphere of Neptune leads to dispersions comparable to those observed by Voyager. The large dispersions are the result of propagation over large distances with wave normal angles very near the resonance cone angle. In the absence of damping, the waves initially propagate approximately along magnetic field lines and drift in magnetic longitude by about 10° per hop. The actual dispersion is clearly dependent on the density along the ray path, which is not known with certainty at this point. For a magnetospheric density model consistent with that suggested by *Gurnett et al.* [1990] we have obtained dispersions of ~ 35,000 s $\sqrt{\text{Hz}}$ for one-hop whistlers. This value of D is comparable to those observed by *Gurnett et al.* [1990] by the plasma wave instrument on board Voyager 2. Our results not only strongly suggest that the signatures observed by *Gurnett et al.* [1990] are in fact whistlers, but make the "requirement" of tens of multiple hops suggested by those authors unnecessary. However, there are still some discrepancies between our results and the observations of Gurnett et al. which we discuss below.

The observations indicate that all of the observed whistlers have approximately the same dispersion. *Gurnett et al.* [1990] suggested that this may be due to longitudinal drift of the ray path of the whistlers from a localized source. We suggest as an alternative to this explanation that only single-hop whistlers from a localized source may exist. Our results indicate that most of the dispersion has occurred by the time the wave has traveled to the magnetic equator. Thus a satellite observing whistlers from a localized source would see a relatively constant dispersion. This does not preclude the existence of multiple-hop whistlers, however.

Another factor that we must consider is the damping of the waves. We can obtain a crude estimate of the possibility of Landau damping by equating the local ionospheric thermal velocity to the parallel phase velocity of the whistler. We do not expect Landau damping outside the ionosphere because the plasma temperature would be much lower. For an ionospheric temperature of about $T = 950°$ [*Tyler et al.*, 1989] we find the critical index of refraction for the onset of Landau damping is given by

$$N_{crit} \sim 2.5 \times 10^3 \cos(\psi) \qquad (8)$$

In the ionosphere of the opposite hemisphere, the ray of Figures 2 and 3 yields $\Psi \sim 42°$, which yields $N_{crit} > 1500$ while the calculated value is $N \sim 25$. For all points along the ray path the largest wave normal angle of the wave is $\Psi \sim 63°$ (Figure 4), which yields $N_{crit} > 1100$. The largest index of refraction of the wave for all points along the ray path is $N \sim 90$. We conclude therefore that no Landau damping is expected.

Most of the whistlers reported by *Gurnett et al.* [1990] were observed near the magnetic equator at a longitude of about 250° with $L < 2$. Our calculations indicate that the largest dispersions should result from whistlers with sources near geographic coordinates of $20° < \lambda < 40°$ and $130° < \Lambda < 150°$. For these sources the ray path intercepts a longitude of ~170° near the magnetic equator, and with $2.5 < L_{avg} < 3.0$. Attempts to make the model whistlers intercept the region of observation yielded a time delay of less than 10 s for one-hop whistlers.

From Figure 4 and Table 1 of *Gurnett et al.* [1990] the total travel time for the observed whistlers in the frequency range of $9 < f < 11$ kHz is seen to be between about 230 s and over 300 s. For all of the cases of this study the total travel time of the waves was less than 100 s, even though the model dispersions are comparable to those observed. This would indicate that the actual ray path or plasma parameters have not been exactly reproduced.

It is our belief that while in this initial study we have not been able to reproduce the observations exactly with regard to location we have shown that extremely large dispersions are to be expected for whistlers at Neptune. These large dispersions are primarily due to a large cold plasma density resulting in propagation near the resonance cone angle over great distances. By modifying the surface magnetic field model and/or the magnetospheric and ionospheric density model, it is quite possible to produce model whistlers that agree with the observations with respect to both location and dispersion. Such a study is most likely tedious, but may also provide an indirect measure of the surface magnetic field strength and cold plasma density, which at this point are still uncertain.

It is also not known at this time exactly what effect higher-order moments of the magnetic field might have on whistler dispersion. We are interested in determining what parameters control if or how rapidly Ψ approaches Ψ_r. At this time we know that higher magnetospheric density in combination with lower magnetic field strength increases the time delay. The initial angle of the wave with respect to the density gradient, the ionospheric and magnetospheric density, and the curvature and strength of the magnetic field all control how rapidly Ψ approaches Ψ_r. The relative importance of each is not well known at this time. We have found, however, that the ionospheric density appears to be the least sensitive of the parameters. We thus believe that magnetic field strength near the source and magnetospheric density are the main factors in producing large delay times and consequently large dispersions.

Acknowledgments. We wish to thank C. Farmer for typesetting and Tony Sawka for drafting. This work was supported by NASA grants NAGW-1205 and NAGW-2412. The work at the University of Iowa was supported by JPL Contract 957723 and by subcontract 15-3667 to SwRI.

The Editor thanks S. L. Moses and U. S. Inan for their assistance in evaluating this paper.

REFERENCES

Barbosa, D.D., W.S. Kurth, I.H. Cairns, D.A. Gurnett, and R.L. Poynter, Electrostatic electron and ion cyclotron harmonic waves in Neptune's magnetosphere, *Geophys. Res. Lett.*, *17*, 1657, 1990.

Belcher, J. W., et al., Plasma observations near Neptune: Initial results from Voyager 2, *Science*, *246*, 1478, 1989.

Cairo, L., and F. Lefeuvre, Localization of sources of ELF/VLF hiss observed in the magnetosphere: Three-dimensional ray tracing, *J. Geophys. Res.*, *91*, 4352, 1986.

Cerisier, J. C., Accessibilité par propagation aux résonances très basse fréquence dans l'ionosphère, *Ann. Geophys.*, *23*, 249, 1967.

Cerisier, J.C., Propagation perpendiculaire au voisinage de la fréquence de la résonance hybride basse, in *Plasma Waves in Space and in the Laboratory*, vol. 2, pp. 487-521, Edinburgh University Press, Edinburgh, 1970.

Gurnett, D. A., W. S. Kurth, R. L. Poynter, L. J. Granroth, I. H. Cairnes, W. M. Macek, S. L. Moses, F. V. Coroniti, C. F. Kennel, and D. D. Barbosa, First plasma wave observations at Neptune, *Science*, *246*, 1494, 1989.

Gurnett, D. A., W. S. Kurth, I. H. Cairns, and L. J. Granroth, Whistlers in Neptune's magnetosphere: Evidence of atmospheric lightning, *J. Geophys. Res.*, *95*, 20967, 1990.

Haselgrove, J., Ray theory and a new method of ray tracking, in *Report of the Conference on the Physics of the Ionosphere*, p. 355, London Physical Society, London, 1955.

Helliwell, R. A., *Whistlers and Related Ionospheric Phenomena*, Stanford University Press, Stanford, Calif., 1965.

Menietti, J. D., H. K. Wong, D. A. Wah, and C. S. Lin, Source region of the smooth high-frequency nightside Uranus kilometric radiation, *J. Geophys. Res.*, *95*, 51, 1990.

Ness, N. F., M. H. Acuna, L. F. Burlaga, J. E. P. Connerney, R. P. Lepping, and F. M. Neubauer, Magnetic fields at Neptune, *Nature*, *246*, 1473, 1989.

Sawyer, C., J.W. Warwick, and J.H. Romig, Smooth radio emission and a new emission at Neptune, *Geophys. Res. Lett.*, *17*, 1645, 1990.

Shinagawa, H., and J. H. Waite, Jr., The ionosphere of Neptune, *Geophys. Res. Lett.*, *16*, 945, 1989.

Stix, T. H., *The Theory of Plasma Waves*, McGraw-Hill, New York, 1962.

Tyler, G. L., et al., Voyager radio science observations of Neptune and Triton, *Nature*, *246*, 1466, 1989.

D. B. Curran and J. D. Menietti, Space Sciences Department, Southwest Research Institute, 6220 Culebra, P. O. Drawer 28510, San Antonio, TX 78228.

D. A. Gurnett and D. Tsintikidis, Department of Physics and Astronomy, University of Iowa, Iowa City, IA 52242.

(Received March 6, 1991;
revised May 28, 1991;
accepted June 19, 1991.)

JOURNAL OF GEOPHYSICAL RESEARCH, VOL. 97, NO. A11, PAGES 17131–17,139, NOVEMBER 1, 1992

Numerical Simulations of Bursty Radio Emissions From Planetary Magnetospheres

R. M. WINGLEE

Geophysics Program, University of Washington, Seattle

J. D. MENIETTI[1] AND H. K. WONG

Department of Space Sciences, Southwest Research Institute, San Antonio, Texas

93A16355

The Voyager spacecraft observed both smooth and bursty radio emissions from Uranus and Neptune. These emissions are known to be freely propagating primarily in the right-hand circularly polarized (RCP) mode with the bursty emissions having burst periods as short as a few tenths of a second and the smooth emissions being observed over periods of a few hours. While the smooth emission is probably due to the electron cyclotron maser instability, some other processes must be at work to produce the bursty emissions. It is proposed that one important difference in mechanisms is that the smooth emissions are associated with continuous injection of electrons while the bursty emissions are associated with impulsive injection. In the latter case, the electron distribution can develop a beam feature with a temperature anisotropy. It is shown via one-dimensional (three velocity) relativistic particle simulations that while the beam may be initially unstable to an electrostatic instability, this instability quickly saturates and eventually the beam is unstable to a strong electromagnetic beam instability which utilizes the temperature anisotropy as free energy; a beam feature is not explicitly needed for the growth of this electromagnetic instability. The radiation generated by the instability is able to convert particle energy to wave energy at similar levels as the maser instability. For $\omega_{pe}/\Omega_e \gtrsim 1$, most of the wave energy is LCP and is trapped. However, for $\omega_{pe}/\Omega_e \lesssim 1$ the dominant mode is RCP. The induced waves are in the form of modified whistlers when the beam speed is low and $\omega_{pe}/\Omega_e \simeq 1$ but are in the freely propagating x mode branch when $\omega_{pe}/\Omega_e \simeq 0.4$. The amount of radiation with frequencies above the local x mode cutoff increases with beam speed. It is also postulated that some of the radiation generated below the local x mode cutoff may also be able to escape the plasma and be detected remotely via mode conversion between regions where field-aligned currents produce local perturbations in the magnetic field.

1. INTRODUCTION

Observations of planetary radio emissions from Uranus and Neptune obtained by the Voyager 2 spacecraft have shown clear evidence of two distinct classes of radiation which are characterized as smooth and bursty. At Uranus, the smooth emission is seen as broadband continuous emissions, from a few kilohertz to about 900 kHz and continuous in time over periods of a few hours. Many studies have suggested that the b-smooth emission is generated by the cyclotron maser instability [e.g., *Kaiser et al.*, 1987; *Menietti et al.*, 1990]. The Uranian broadband bursty (b-bursty) emission is seen in the range 300-700 kHz and occurs at times which are intermediate between the observations of the smooth emissions (see Plate 1 of *Farrell and Calvert* [1989] for an excellent graphical display). Thus the smooth and bursty emissions are quite distinct in frequency range, duration, and spacecraft event time. Uranian narrowband bursty (n-bursty) emissions show further frequency and temporal fine structure [*Farrell et al.*, 1990].

[1]Now at Department of Physics and Astronomy, University of Iowa, Iowa City.

Paper number 92JA01521.
0148-0227/92/92JA-01521$05.00

Many early studies based on straight-line propagation [cf. *Leblanc et al.*, 1987; *Farrell and Calvert*, 1989] indicated the source of the b-bursty emission was colocated with the smooth emission near the south magnetic pole. These early studies generally agree that the emission propagates at large wave normal angles and suggest the cyclotron maser instability (CMI) as the source mechanism. However, *Curran et al.* [1990] have shown, via a ray tracing study, that refractive effects are important and that the source of the bursty emissions appears to be at lower latitudes for emission initially propagating at large wave normal angles. The conclusion of this latter study was that since the source region is different from that of the b-smooth emission, it is possible that the emission may be due to a distinct plasma distribution at lower latitudes and/or a different source.

Observations of the radio emission obtained by the Voyager 2 flyby of Neptune also show clear examples of both a bursty and a smooth component [e.g., *Warwick et al.*, 1989; *Farrell et al.*, 1990]. The bursty emission is observed between 500 kHz and 1.3 MHz while the smooth emission is seen in the frequency range $f < 500$ kHz. The bursty emission is also generally observed at distinct times from the smooth emission, and their source regions appear to be different [*Farrell et al.*, 1990; *Ladreiter et al.*, 1991]. The emission appears to occur in episodes with strong bursts of duration < 6 s,

PRECEDING PAGE BLANK NOT FILMED

and the polarization is consistent with the right-hand extraordinary mode. Generally the bandwidth of the Neptune bursty emission is much shorter than that of the b-bursty emission at Uranus, with the former having a bandwidth of less than 20 kHz.

It has been suggested that both the smooth and bursty emissions are due to the electron cyclotron emissions, similar to the proposal for the emissions at Uranus [e.g., *Farrell et al.*, 1990 and references therein]. However, the above differences in the characteristics of the smooth and bursty emissions suggest that there are distinct emission mechanisms at work and/or that there are distinct differences in the plasma conditions in the source region.

Recently, *Wong and Goldstein* [1990] suggested that the bursty radio emissions from planetary magnetospheres could be due to a temperature anisotropic beam instability (hereafter called TABI). This mechanism is essentially the same as the early proposal by *Melrose* [1976] for the generation of auroral kilometric radiation (AKR) and Jupiter's decametric radiation (DAM), which have many similarities to the smooth emissions seen at Uranus and Neptune. However, general interest in this instability rapidly faded when *Wu and Lee* [1979] developed the theory for the electron cyclotron maser instability. This maser instability, which is driven by a population inversion in the electron perpendicular velocity (i.e., $\partial f/\partial v_\perp > 0$), is able to provide a ready explanation for many of the observed features of AKR and DAM, including frequency cutoff of the excited radiation, their polarization and brightness temperature, and the overall characteristics of the electron distribution in the nightside auroral region.

Nevertheless, there is growing evidence that the types of distributions required to drive the TABI can also be present, at least on occasions [*Menietti and Burch*, 1991]. There is also some recent evidence from laboratory experiments that the TABI can be generating bursty electromagnetic radiation [*Urrutia and Stenzel*, 1984; *Goldman and Newman*, 1987]. The TABI differs from the maser instability in that it is driven by a temperature anisotropy where $T_\perp \gg T_\parallel$ and no explicit positive gradients (i.e., inverted populations) need be present. It is similar to the maser instability in that it still involves generation of electromagnetic radiation via a gyroresonant wave-particle interaction. *Newman et al.* [1988] subsequently performed a comprehensive study of the mechanism including numerical simulations for the case when the ratio of the plasma frequency (ω_{pe}) to gyrofrequency (Ω_e) was greater than 2.5. *Wong and Goldstein* [1990] have extended the theory to the region of $\omega_{pe}/\Omega_e \lesssim 1$ typical of planetary magnetospheres. They showed that the TABI can easily generate radiation as much as a factor of 2 above the electron cyclotron frequency, with the radiation being beamed into a filled emission cone of half-angle less than 30°.

In this paper one-dimensional relativistic particle-in-cell simulations are used to investigate the radiation from electron beams with a large temperature anisotropy for conditions relevant to planetary magnetospheres. The use of simulations is critical to the problem because these types of distribution are not only unstable to the TABI but also to electrostatic beam instabilities which generate Langmuir waves. These two instabilities compete for and modify the free energy in the distribution as they try and reduce the gradients in the distribution. This competition between instabilities is neglected in all the above theoretical treatments of the TABI. It is shown that these beams, which would typically originate from the sporadic or impulsive injection of energetic electrons, can generate electromagnetic radiation which should be able to escape into the solar wind despite the growth of the electrostatic instability. This escaping radiation is most likely generated under conditions when the ratio of the electron plasma frequency ω_{pe} to the electron cyclotron frequency Ω_e is between about 0.3 and 1.0. The efficiency increases with energy of the beam electrons. This parameter regime complements that required for the maser instability, which tends to be restricted to $\omega_{pe}/\Omega_e \lesssim 0.3$. Thus the TABI provides a natural explanation for the apparent differences in source location and spacecraft event times between the smooth and bursty emissions.

2. Comparison Between Maser and Beam Instabilities

The processes that may be involved in the generation of both the smooth and bursty emissions are illustrated in Figure 1. The standard model for producing the smooth emissions is shown in Figure 1a. Because of the long duration of the smooth emissions, there must be a continual resupply of the energetic electrons producing the radiation; otherwise the driving mechanism would quickly saturate and the emissions would cease. For such a continual flow of energetic electrons down the field lines a loss cone distribution would form, as electrons with large pitch angles mirror and move back up the field lines while electrons with small pitch angles precipitate out of the flux tube and are lost to the lower atmosphere. Such loss cone distributions are unstable to the maser instability, which generates the observed radiation for the smooth emissions.

For the bursty emissions, the physics involved is substantially different. In particular, the presence of short bursts implies that the energetic electrons responsible for the emissions are being injected intermittently. For rapid or impulsive injection, only certain particles can reach a point further down the field line at any particular time, since slow particles would not have had sufficient time to reach it and fast particles would have already passed by [e.g., *White et al.*, 1986; *Winglee and Dulk*, 1986]. This velocity filtering occurs irrespective of the initial distribution, which could be beamlike or just a hot Maxwellian of solar wind origin. As a result of these time-of-flight effects, the local distribution can be narrowly confined in the parallel velocity, allowing the distribution to develop a beamlike feature. Furthermore, since the time-of-flight effects depend only weakly on the perpendicular velocity (assuming only weak magnetic field convergence), the particles arriving at any particular point can have a much larger spread in their perpendicular velocity than in their parallel velocity, effectively giving the beam a temperature anisotropy.

Note that these types of distributions can develop from the same initial distribution as that driving the loss cone formation; the main difference in the evolution of the

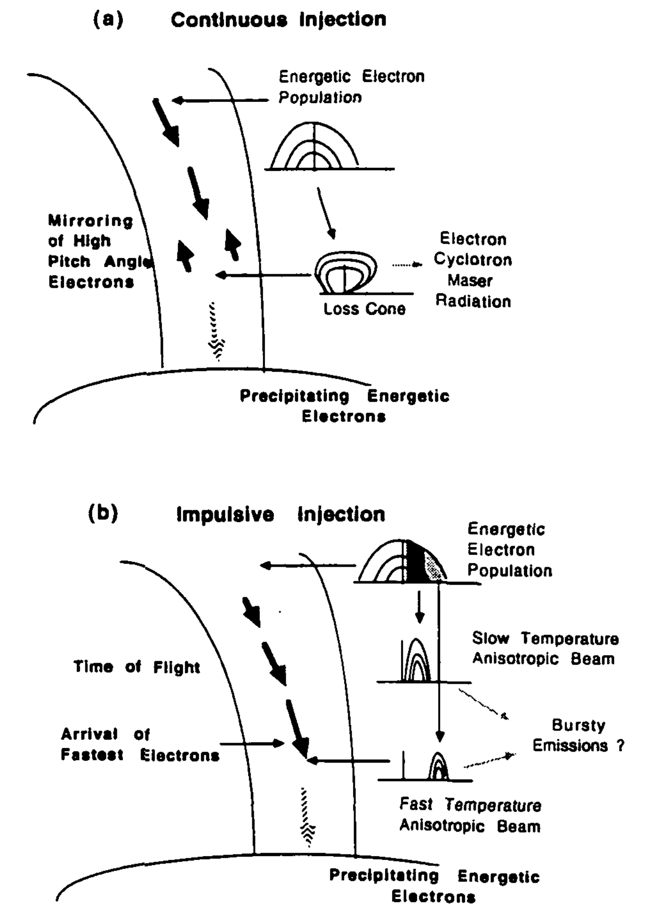

Fig. 1. Schematic showing (a) the development of a loss cone distribution during continuous injection of energetic electrons and the subsequent generation of maser emission responsible for the smooth emissions and (b) the development of a temperature anisotropic beam during impulsive injection. This type of beam can drive a modified Weibel instability or TABI which can generate radiation which can possibly account for the bursty emissions.

distribution arises from the injection period relative to the transit time of the particles along the flux tube. For loss cones to develop, the injected period must be much longer than the transit time, i.e., at least greater than about a few minutes. Temperature anisotropic beams would probably be generated if the injection occurs sporadically with each burst having a period smaller than about a minute or so.

When a temperature anisotropic beam develops, a modified kinetic "Weibel instability" [*Newman et al.*, 1988] or TABI can develop which grows off the difference in gradients between the perpendicular and parallel velocities. The instability does not explicitly need a positive gradient in the distribution (unlike the maser instability) although a positive gradient associated with the beam component is often assumed in theoretical treatments. When the ratio of the plasma frequency ω_{pe} to the electron cyclotron frequency Ω_e is much greater than 1, modified whistlers are excited [*Newman et al.*, 1988]. However, if $\omega_{pe}/\Omega_e < 1$, then *Wong and Goldstein* [1990] predict that the dominant emission is in the right-hand circularly polarised (RCP) x mode with $\omega > \Omega_e$, and it is this radiation which they propose as the possible source of the bursty planetary emissions. In the following, the nonlinear evolution of the TABI is examined through particle simulations in order to compare its characteristics with that of the maser instability and, thereby, provide better insight into the possible origins of the bursty and smooth emissions.

3. Particle Distributions and Particle Heating

The nonlinear evolution of the temperature anisotropic beam instability is investigated via one-dimensional (three velocity) relativistic electromagnetic particle simulations [cf. *Newman et al.*, 1988]. This code solves self-consistently the full set of Maxwell's equations and allows the evaluation of the competition between electromagnetic and electrostatic beam instabilities. The system is assumed to be periodic with the wave vector k directed along the magnetic field, which is in the x direction. The size of the system L is assumed to be 1024 Debye lengths, and the corresponding wavenumber of a mode m in the system is then $2\pi m/L$.

In all the following simulations the density of the plasma is kept constant and the magnetic field strength is varied so that ω_{pe}/Ω_e ranges from a maximum value of 2.5 down to a minimum value of 0.25. This parameter regime extends that considered by *Newman et al.* [1988] where only values of $\omega_{pe}/\Omega_e \geq 2.5$ were considered.

The plasma is assumed to consist of (1) a cold ambient plasma with a Maxwellian distribution with a thermal speed v_{Tc} equal to 0.04c, which comprises 90% of the total electron density, and (2) a beam component with a parallel temperature the same as the cold component

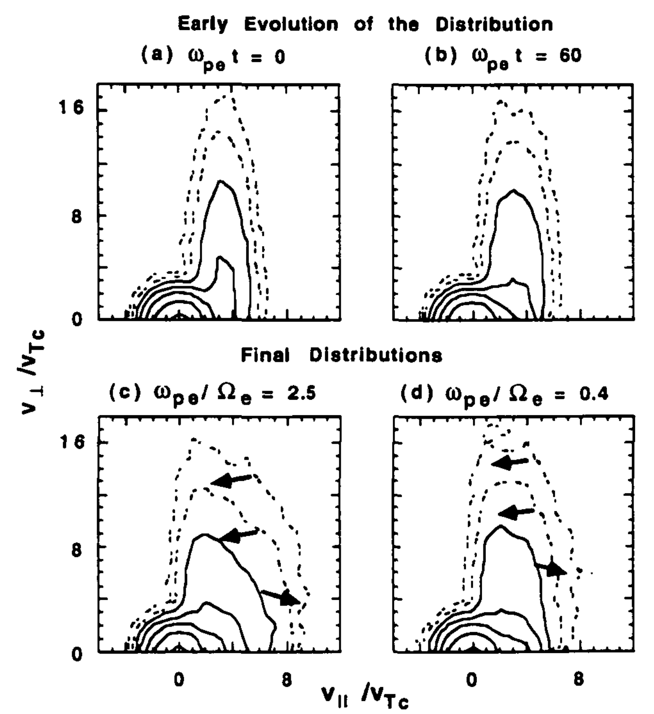

Fig. 2. The evolution of the total electron distribution for $v_b = 4v_{Tc}$. (a) The initial distribution. (b) The early development of a weak electrostatic beam instability causes some parallel heating. (c) and (d) The strongest heating is driven by the TABI which produces scattering in both pitch angle and energy, as indicated by the arrows. This latter heating is dependent on ω_{pe}/Ω_e while the heating by the electrostatic instability is not.

and a perpendicular temperature 36 times the parallel temperature, i.e., $v_{T\|E} = v_{Tc}, v_{T\perp E} = 6v_{T\|E}$. This latter component makes up the remaining electron plasma density, i.e., 10% of the total electron density. These parameters are similar to those used by *Newman et al.* [1988]. Three different beam speeds v_b are considered: v_b equal to 4, 6, and 8 v_{Tc}.

The initial distribution comprising these two components for $v_b = 4v_{Tc}$ is shown in Figure 2a. It is unstable to both the electromagnetic beam instability and a weak electrostatic beam instability (similar to the normal bump-in-tail instability). The electrostatic instability quickly saturates (by $\omega_{pe}t \simeq 60$) and produces only some flattening of the distribution in the range $3 \lesssim v_\|/v_{Tc} \lesssim 4$ (Figure 2b). Most of the particle heating is driven by the electromagnetic beam instability, as illustrated in Figures 2c and 2d which show the velocity distributions at saturation ($\omega_{pe}t \simeq 1000$) for ω_{pe}/Ω_e equal to 2.5 and 0.4, respectively.

The electromagnetic instability acts on the distribution in an effort to reduce the temperature anisotropy. For $\omega_{pe}/\Omega_e \gtrsim 1$ (Figure 2c), this isotropization is achieved in two ways: (1) low pitch angle electrons are scattered forward to higher $v_\|$ and (2) high pitch angle electrons are scattered to lower pitch angles and lower energies. For $\omega_{pe}/\Omega_e \lesssim 1$, the beam particles primarily experience only scattering to lower pitch angles, and the acceleration of low pitch angle particles to higher energies is significantly reduced. This change in the heating of the particle distribution is due to the development of different unstable modes as ω_{pe}/Ω_e is varied (see section 4).

Figure 3 shows the temporal evolution of the distribution when the beam speed is increased to $6v_{Tc}$ and ω_{pe}/Ω_e is held fixed at 2/3. Because of the higher beam speed, the electrostatic instability is very much stronger and quickly flattens the beam feature in $v_\|$, as seen in Figures 3a and 3b. As a result of the growth of this instability, the distribution no longer has a positive slope anywhere. Despite this flattening of the beam feature, there are still large temperature anisotropies (i.e., $\partial f/\partial v_\perp \ll \partial f/\partial v_\|$) on both the leading and trailing edges of the beam feature. It is this temperature anisotropy which drives the TABI at later times and produces the continued heating of the particle distribution (Figures 3c and 3d), similar to Figure 2. Note that, unlike the maser instability, a population inversion is not required for the growth of the TABI.

The time history of the energy going into the electrostatic waves is shown in Figure 4 for the three different assumed beam speeds. The electrostatic wave energy for a given beam speed did not vary significantly for the different magnetic field strengths (i.e., ω_{pe}/Ω_e) considered, since the electrostatic waves are generated by a Landau resonance and not by a gyroresonance. It is seen that the peak energy going into these waves increases with increasing beam speed. However, in all cases this wave energy is mostly reabsorbed as the particle distribution evolves from one which has a positive slope in $v_\|$ to one in which such positive slopes are absent. The growth and reabsorption of these waves occurs on relatively fast time scales, within about $\omega_{pe}t \lesssim 200$.

The corresponding amount of energy being converted to electromagnetic wave energy is shown in Figure 5. The electromagnetic wave energy differs from the electrostatic

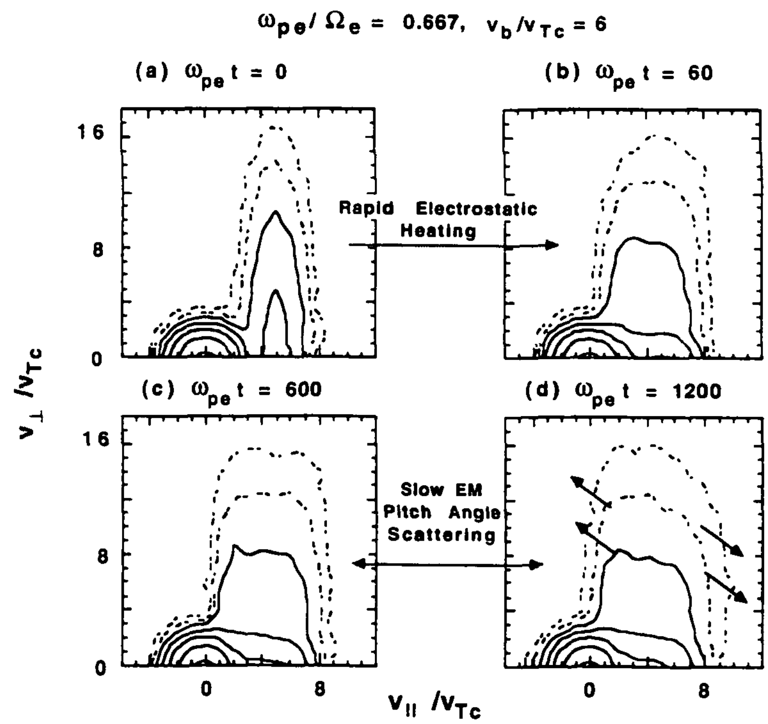

Fig. 3. The temporal evolution of the electron distribution for $v_b = 6v_{Tc}$ and $\omega_{pe}/\Omega_e = 2/3$. Because of the increased beam speed there is much strong parallel heating of the electron distribution via the electrostatic beam instability. However, at late times (in Figures 3c and 3d) the TABI is still able to grow and produce further particle scattering in pitch angle and energy.

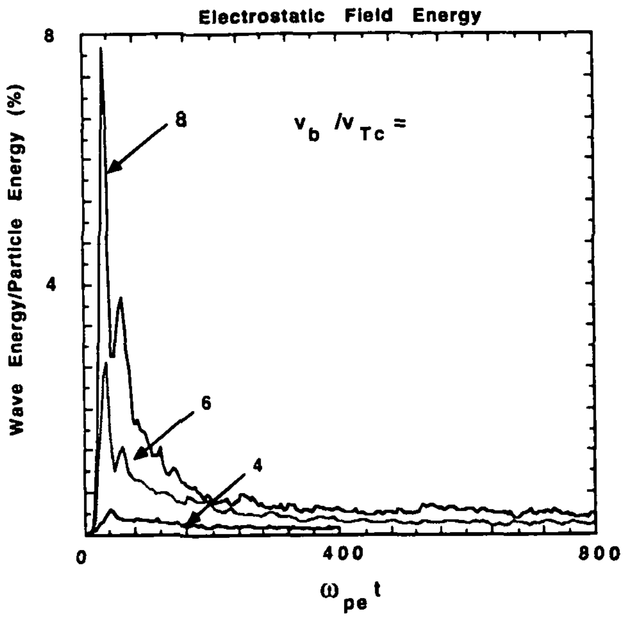

Fig. 4. The time history of the particle energy being converted into electrostatic wave energy. Irrespective of the beam speed, the energy rapidly increases and is then reabsorbed.

wave energy in three ways. First, it grows on much longer time scales than the electrostatic wave energy. Indeed, there is a tendency for the electromagnetic waves to have to wait until the electrostatic waves have saturated and been reabsorbed before the TABI becomes intense. This delay arises because the fast growing electrostatic instability modifies the electron distribution, which in turn tends to destroy the slower growing gyroresonant interactions. Second, the bulk of the wave energy is not reabsorbed. Third, the efficiency depends strongly on the value of ω_{pe}/Ω_e.

For the lowest beam speed, the efficiency increases with increasing ω_{pe}/Ω_e (Figure 5a). As the beam speed is increased to $v_b = 6v_{Tc}$ (Figure 5b), the overall efficiency is larger with peak efficiency increasing about 10% for $\omega_{pe}/\Omega_e \simeq 2/3$. For $v_b = 8v_{Tc}$ (Figure 5c), the maximum efficiency is about the same but occurs at a lower value of ω_{pe}/Ω_e, equal to about 1/2. This change in the efficiency is consistent with the increase in the predicted growth rate for increasing beam speed [cf. *Wong and Goldstein*, 1990].

The efficiencies shown in Figure 5 of a few percent are comparable to that of the maser instability [e.g., *Pritchett*, 1986]. In other words, the TABI under certain conditions can produce radiation as intense as the maser instability. However, the two instabilities occur in different but complementary plasma regimes. Specifically, the maser instability is know to be relatively strong for $\omega_{pe}/\Omega_e \lesssim 0.3$ while the above results show that the TABI is primarily effective for $\omega_{pe}/\Omega_e \gtrsim 0.3$.

It should be noted that the above simulations treat the system as homogeneous so that the true efficiency of the instability may be strongly modified by inhomogeneities in the actual source region of a planetary magnetosphere. This is also true for the maser instability. For example, wave propagation out of the source may limit the amplification of the wave. On the other hand, particle propagation effects may help maintain the initial distribution, as heated particles move out and new particles propagate into the source region. As a result, the instability may be sustained over many e-folding periods rather than quickly reaching saturation as the gradients in the distribution are eroded. Evaluation of these competing effects needs detailed information about the source region which is currently not available.

4. CHARACTERISTICS OF THE WAVE SPECTRUM

The characteristics of the excited waves are expected to change as ω_{pe}/Ω_e is varied from above to below unity.

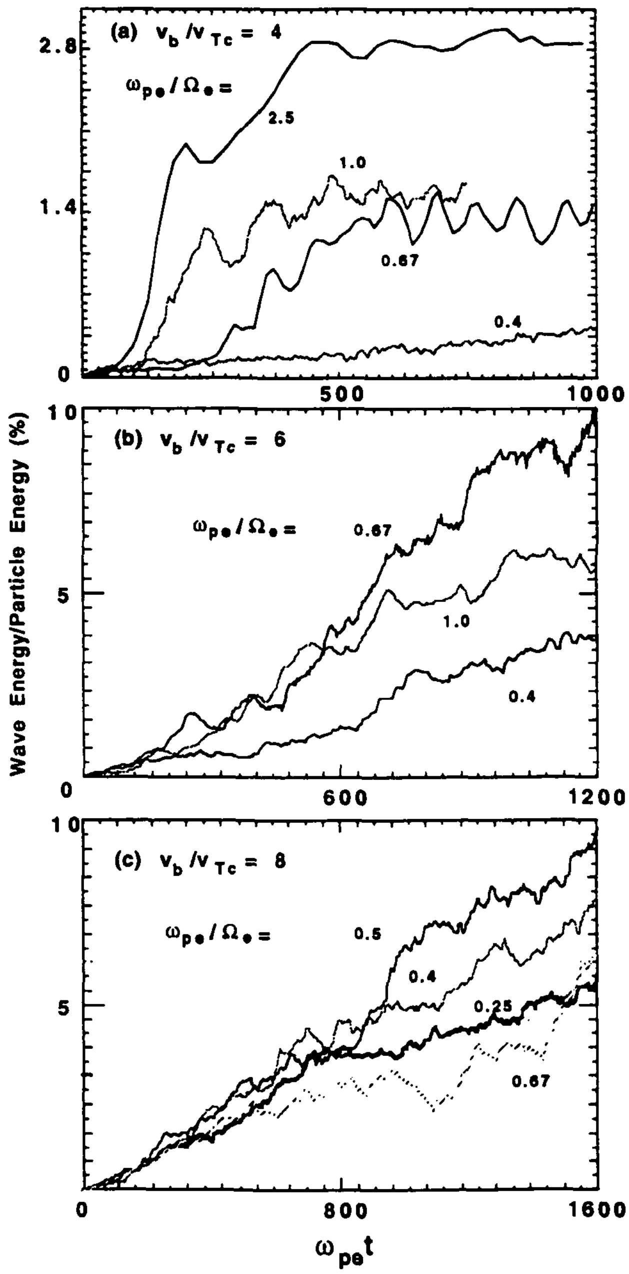

Fig. 5. The time history of the energy going into the electromagnetic wave for the different values of beam speed and ω_{pe}/Ω_e. As the beam speed is increased beyond a few thermal speeds, the efficiency increases to a maximum of about 10%. This peak efficiency is, however, attained over longer periods and lower values of ω_{pe}/Ω_e.

In particular, for $\omega_{pe}/\Omega_e \gtrsim 1$, the whistler can have a frequency comparable to the electron cyclotron frequency due to a Doppler shift associated with the presence of the beam. This Doppler shift allows gyroresonant interactions to occur. However, when $\omega_{pe}/\Omega_e \lesssim 1$, the maximum frequency of the whistler is limited to ω_{pe}, where it becomes increasingly electrostatic so that gyroresonant interactions are suppressed. However, the cutoff for the x mode and resonance for the z mode start to approach the cyclotron frequency, and it is these modes which can then become unstable through gyroresonant interactions if the beam velocity is large enough. This change in the mode structure is illustrated in this section.

Figure 6 shows the spectrum derived from integrating the power in the different k modes over the full period of the simulations for $v_b/v_{Te} = 4$. In order to separate spectra from different modes, some of the lines have been dotted. It is seen that, for $\omega_{pe}/\Omega_e = 2.5$, the dominant emission is at about 0.5 Ω_e and is left-hand polarised (LCP). This mode is essentially a beam-modified backward propagating whistler. Because its frequency is below Ω_e, this emission is expected to be trapped in a planetary magnetosphere.

At the intermediate values of ω_{pe}/Ω_e (Figures 6b and 6c), there is still relatively strong emission at 0.5 Ω_e. In addition, strong emissions appear at frequencies slightly above Ω_e. This is the RCP x mode predicted by *Wong and Goldstein* [1990], and it is this radiation, particularly for the lower values of ω_{pe}/Ω_e, which can possibly escape into the solar wind and produce the bursty emissions. However, in the present case the beam speed is small, and most of the wave energy has frequencies below the local x mode cutoff and cannot directly escape the plasma. Only at the lowest value of ω_{pe}/Ω_e shown is there a small tail ($\approx 1\%$ of the electromagnetic energy) with frequencies above the local x mode cutoff.

Nevertheless, there is still a possibility that some of the radiation can escape because the electron injection must be associated with development of field-aligned currents. These currents can produce perturbations in the magnetic field of a few percent of the local ambient magnetic field in the nightside auroral region, and there is no reason to believe that such magnetic perturbations

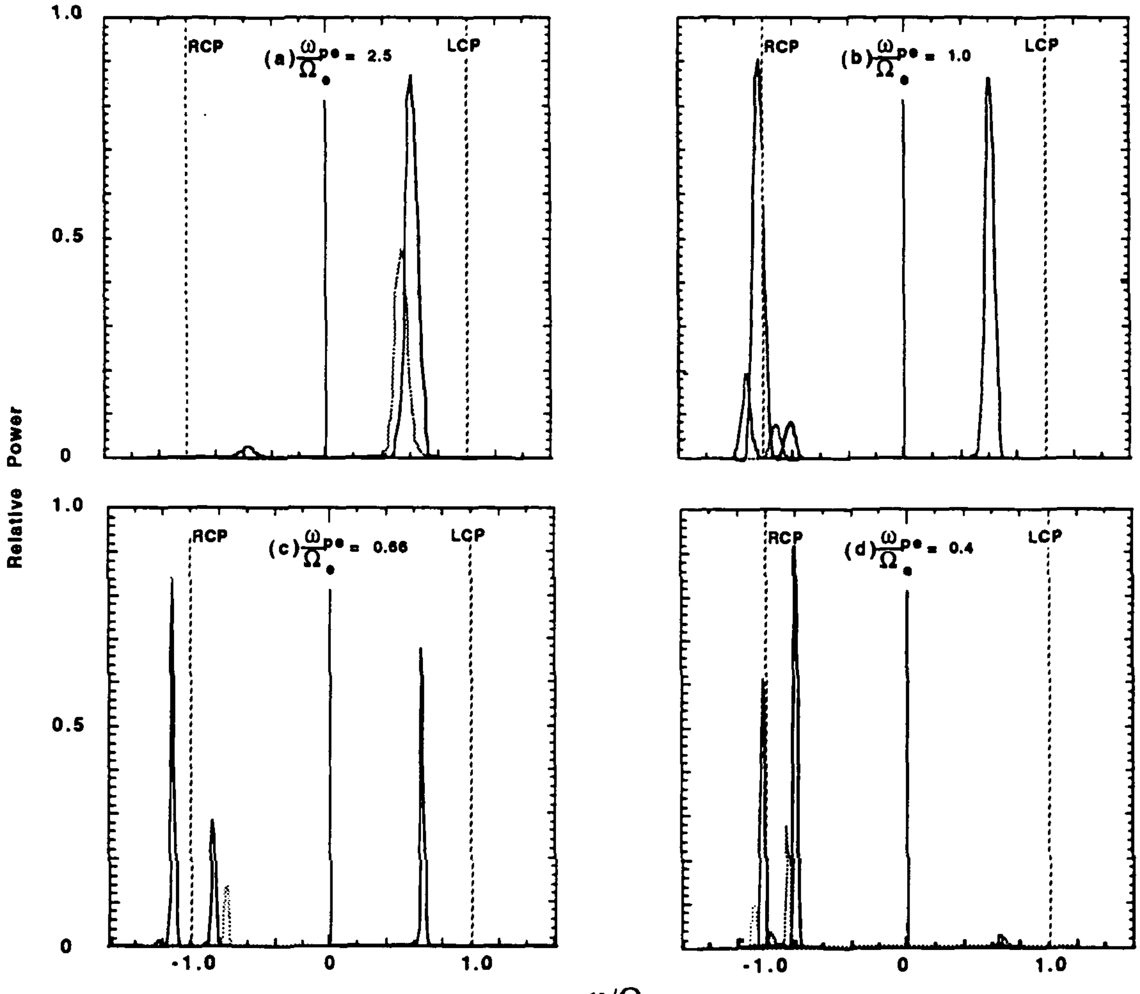

Fig. 6. The frequency spectrum of the different k modes when $v_b/v_{Te} = 4$ and for the four different ω_{pe}/Ω_e. Some of the spectra appear as dotted lines in order to highlight differences between modes. For $\omega_{pe}/\Omega_e \gtrsim 1$, the dominant mode is LCP. However, as ω_{pe}/Ω_e is decreased, the RCP waves become relatively more intense with a significant portion above Ω_e but below the x mode cutoff. Only in Figure 6d is there a weak tail in the spectrum with frequencies above the x mode cutoff.

should not also be present in the magnetospheres of the outer planets. Such perturbations could modify the local cyclotron and cutoff frequencies so that they temporarily fall below the frequency of the excited radiation. In this case, mode conversion of the induced TABI radiation can allow the escape of some of the radiation, even for this relatively low beam speed.

As the beam speed is increased, a larger portion of x mode waves is generated with frequencies above the local x mode cutoff. As an example, Figure 7 shows the spectra for $v_b/v_{Te} = 6$ and for three values of ω_{pe}/Ω_e where the relative efficiency of the TABI is near its maximum. It is seen that emissions in the LCP mode are all but suppressed and that the dominant emissions are in the RCP mode with frequencies above the cyclotron frequency. Moreover, for the smallest value of ω_{pe}/Ω_e shown, the dominant emission has a frequency above the x mode cutoff which is denoted by ω_x in the figure.

Further increases in the beam speed (Figure 8) produce

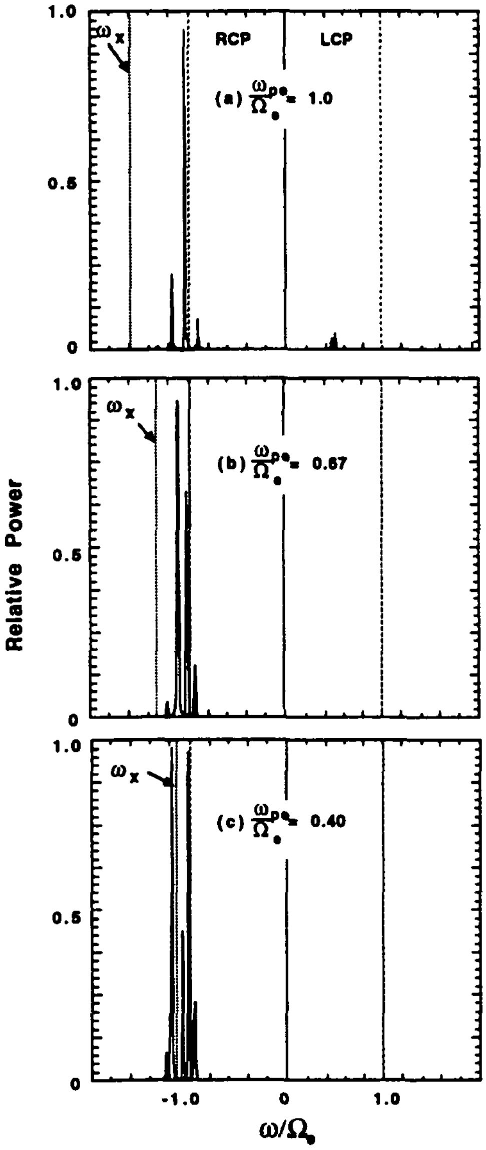

Fig. 7. As in Figure 6 but for $v_b/v_{Te} = 6$. For this higher beam speed the radiation with frequencies above the x mode cutoff ω_x actually dominates the spectrum at the lowest value of ω_{pe}/Ω_e shown.

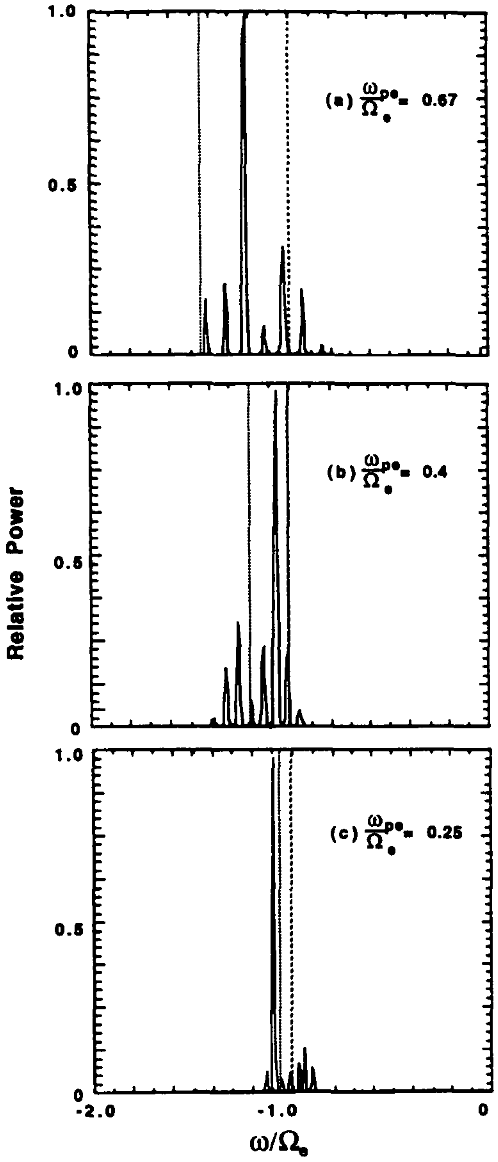

Fig. 8. As in Figure 6 but for $v_b/v_{Te} = 8$. There is a further upshift in the frequency spectrum with more of the radiation appearing above ω_x, and the growth of all the LCP waves is suppressed.

a continuing upshift in the frequency of the dominant modes. For the highest value of ω_{pe}/Ω_e shown (Figure 8a), the upper cutoff of the excited radiation is nearly 1.5 Ω_e compared with only about 1.17 Ω_e in Figure 6. At smaller values of ω_{pe}/Ω_e a growing fraction of the wave energy is above the x mode cutoff.

Note that while the frequency of the excited radiation is increasing with beam speed, it increases at a smaller rate than predicted by *Wong and Goldstein* [1990]. This difference arises from the presence of the fast growing electrostatic waves which are not included in the linear theory of *Wong and Goldstein* [1990]. These waves tend to cause a reduction in the average drift speed of the energy beam particles and hence in the Doppler shift.

5. CONCLUSIONS

One-dimensional electromagnetic particle simulations have been used to evaluate the characteristics of radiation from electron beams with temperature anisotropies in order to identify the origin of bursty planetary emissions. Such beams can arise for example during the impulsive or sporadic injection of energetic electrons in which time-of-flight effects restrict the parallel velocity of the particles arriving at any specific point and time down the field lines. Terrestrial observations show that such temperature anisotropies in association with electron beams can indeed be present at least in the Earth's auroral region [cf. *Menietti and Burch*, 1991]. In contrast, the smooth planetary emissions are believed to be generated by the cyclotron maser instability (CMI), which is presumably driven by the continuous injection of the energetic electrons and the subsequent development of loss cone distributions.

These temperature anisotropic beams are unstable to a modified kinetic Weibel or temperature anisotropic beam instability (TABI). For $\omega_{pe}/\Omega_e \gtrsim 1$, most of the wave energy generated is LCP with frequencies below the cyclotron frequency and is therefore trapped. However, for $\omega_{pe}/\Omega_e \lesssim 1$ the dominant mode is RCP, either in the form of a modified whistler or in the x mode. The latter radiation is strongest for $0.25 \lesssim \omega_{pe}/\Omega_e \lesssim 0.5$ and where beam speed is much greater than the ambient thermal velocity. Under these conditions, the excited radiation can directly escape from the plasma and be detected remotely by a spacecraft. At moderate values of ω_{pe}/Ω_e (i.e., between about 0.5 and 1.0), much of the excited radiation is below the x mode cutoff, and the only possibility for the radiation to escape is via mode conversion across adjacent regions where the magnetic field is locally lower. Such perturbations in the magnetic field may indeed be present since field-aligned currents are likely to be associated with the electron injection. Detailed modeling of these latter processes still needs to be performed in order to establish the exact maximum value of ω_{pe}/Ω_e for which the TABI radiation will be trapped in planetary magnetospheres.

In addition, the TABI is able to convert particle energy into electromagnetic energy with similar efficiencies as the maser instability. As a result, the escaping radiation from the TABI, particularly when $\omega_{pe}/\Omega_e \simeq 0.4$, should have a comparable intensity to that of the maser radiation, which is strongest in regions where $\omega_{pe}/\Omega_e \lesssim 0.3$.

Thus the above features of the TABI radiation strongly complement those of the maser radiation, both in the plasma conditions in which escaping radiation is generated and in the injection of the energetic electrons as it changes from continuous to sporadic. This complementary nature provides a ready explanation for the apparent offsets in source location and spacecraft event time of the smooth and bursty emissions, as well as their different spectral characteristics.

The model presented here suggests a radiation pattern

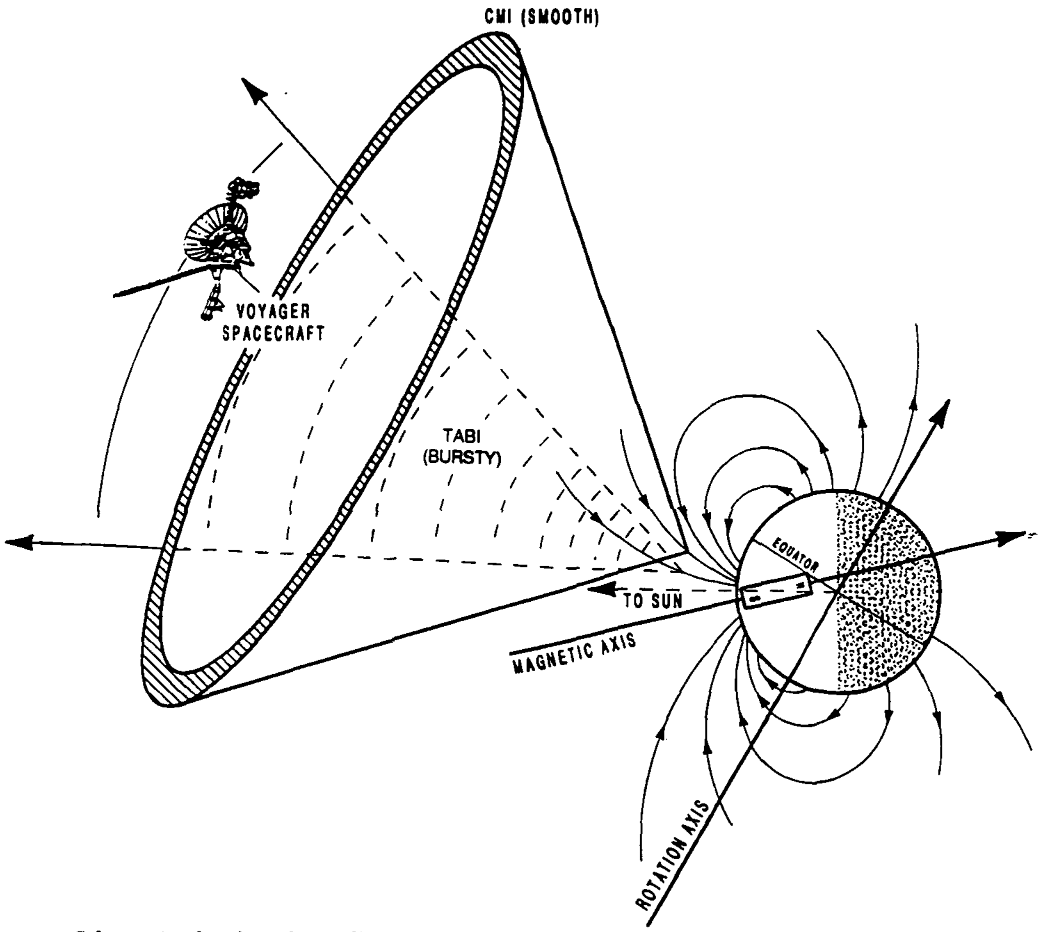

Fig. 9. Schematic showing the radiation pattern in the proposed model for the configuration applicable to Neptune. Radiation from the cyclotron maser emission (CMI) in a hollow cone generates the smooth emissions while the temperature anisotropic beam instability (TABI) generates radiation in a displaced solid cone to produce the bursty emissions.

and source location similar to those shown in Figure 9, with the source regions of the two emissions approximately adjacent, as ω_{pe}/Ω_e and the characteristics of the electron injection vary across the polar regions. As a result of the different emission mechanisms and their source location, a spacecraft would be expected to see the two sides of the hollow cone of the smooth emissions followed by a single patch of bursty emission associated with emission from a filled cone, similar to the observations of *Farrell and Calvert* [1989].

Acknowledgments. This research was supported by NASA grants NAGW-2471, NAGW-2412 and NAGW-1936 and NSF grant ATM 91-96132 and by Southwest Research Institute Internal Research grants 15-9668 and 15-9677. The simulations were performed on the CRAY Y-MP at the San Diego Supercomputing Center which is funded by the National Science Foundation.

The Editor thanks W. M. Farrell and D. B. Melrose for their assistance in evaluating this paper.

REFERENCES

Curran, D. B., J. D. Menietti, and H. K. Wong, Ray tracing of broadband bursty radio emissions from Uranus, *Geophys. Res. Lett.*, *17*, 109, 1990.

Farrell, W. M., and W. Calvert, The source location and beaming of broadband bursty radio emissions from Uranus, *J. Geophys. Res.*, *94*, 217, 1989.

Farrell, W. M., M. D. Desch, and M. L. Kaiser, Field-independent source localization of Neptune's radio bursts, *J. Geophys. Res.*, *95*, 19143, 1990.

Goldman, M. V., and D. Newman, Electromagnetic beam modes driven by anisotropic electron streams, *Phys. Rev. Lett.*, *58*, 1849, 1987.

Kaiser, M. L., M. D. Desch, and S. A. Curtis, The sources of Uranus' dominant nightside radio emissions, *J. Geophys. Res.*, *92*, 15169, 1987.

Ladreiter, H. P., Y. Leblanc, G. K. F. Rabl, and H. O. Rucker, Emission characteristics and source location of smooth Neptunian kilometric radiation, *J. Geophys. Res.*, *96*, 19101, 1991.

Leblanc, Y., M. G. Aubier, A. Ortega-Molina, and A. Lecacheux, Overview of the Uranian radio emissions: Polarization and constraints on source locations, *J. Geophys. Res.*, *92*, 15125, 1987.

Melrose, D. B., An interpretation of Jupiter's decametric radiation and the terrestrial kilometric radiation as direct amplified gyroemission, *Astrophys. J.*, *207*, 651, 1976.

Menietti, J. D., and J. L. Burch, Particle acceleration in the auroral region as observed by DE-1, paper presented at Chapman Conference on Auroral Plasma Dynamics, AGU, Minneapolis, Minn., Oct. 21-25, 1991.

Menietti, J. D., H. K. Wong, D. A. Wah, and C. S. Lin, Source region of the smooth high frequency nightside Uranus kilometric radiation, *J. Geophys. Res.*, *95*, 51, 1990.

Newman, D., R. M. Winglee, and M. V. Goldman, Theory and simulation of electromagnetic beam modes and whistlers, *Phys. Fluids*, *31*, 1515, 1988.

Pritchett, P. L., Electron-cyclotron maser instability in relativistic plasmas, *Phys. Fluids*, *29*, 2919, 1986.

Urrutia, J. M., and R. L. Stenzel, New electromagnetic mode in a non-Maxwellian high-beta plasma, *Phys. Rev. Lett.*, *53*, 1901, 1984.

Warwick, J. W., et al., Voyager planetary radio astronomy at Neptune, *Science*, *246*, 1498, 1989.

White, S. M., D. B. Melrose, and G. A. Dulk, Electron cyclotron masers during solar flares, *Astrophys. J.*, *308*, 424, 1986.

Winglee, R. M., and G. A. Dulk, The electron-cyclotron maser instability as the source of solar type V continuum, *Astrophys. J.*, *310*, 432, 1986.

Wong, H. K., and M. L. Goldstein, A mechanism for bursty radio emission in planetary magnetospheres, *Geophys. Res. Lett.*, *17*, 2229, 1990.

Wu, C. S., and L. C. Lee, A theory of the terrestrial kilometric radiation, *Astrophys. J.*, *230*, 621, 1979.

J. D. Menietti, Department of Physics and Astronomy, University of Iowa, Iowa City, IA 52242.

R. M. Winglee, Geophysics Program AK-50, University of Washington, Seattle, WA 98195.

H. K. Wong, Department of Space Sciences, P.O. Drawer 28510, Southwest Research Institute, San Antonio, TX 78228-0510.

(Received November 25, 1991;
revised June 10, 1992;
accepted June 10, 1992.)

H. O. RUCKER, S. J. BAUER, and M. L. KAISER

(Editors)

PLANETARY RADIO EMISSIONS III

Proceedings of the
3rd International Workshop
held at Graz, Austria
September 2–4, 1991

Separata

VERLAG DER
ÖSTERREICHISCHEN AKADEMIE DER WISSENSCHAFTEN
A-1010 WIEN, DR.-IGNAZ-SEIPEL-PLATZ 2

N/S

NUMERICAL SIMULATIONS OF BURSTY PLANETARY RADIO EMISSIONS

R. M. Winglee*, J. D. Menietti*, and H. K. Wong*

Abstract

The Voyager spacecraft observed both smooth and bursty radio emissions from Uranus and Neptune. These emissions are known to be freely propagating primarily in the right hand circularly polarized mode (RCP) with the bursty emissions having burst periods as short as a few tenths of a second and the smooth emissions being observed over periods of a few hours. While the smooth emission is probably due to the electron cyclotron maser instability some other processes must be at work to produce the bursty emissions. It is proposed that one important difference in mechanisms is that the smooth emissions are associated with continuous injection of electrons while the bursty emissions are associated with impulsive injection. In the latter case, the electron distribution can develop a beam feature with a temperature anisotropy which is unstable to an electromagnetic beam instability that can generate bursty emissions. The characteristics of this radiation is determined via one dimensional (three velocity) particle simulations. It is shown that the electromagnetic beam instability anisotropy is as efficient as the maser instability in converting particle energy to wave energy. For $\omega_{pe}/\Omega_e \gtrsim 1$, most of the wave energy is LCP but is trapped. However, for $\omega_{pe}/\Omega_e \lesssim 1$ the dominant mode is RCP and freely propagating. Furthermore, the radiation is bursty in nature due to the competition between different modes and is most intense when $0.4 \lesssim \omega_{pe}/\Omega_e \lesssim 1$. This regime complements that of the maser emission which is expected to be most intense when $\omega_{pe}/\Omega_e \lesssim 0.3$.

1 Introduction

Observations of planetary radio emissions from Uranus and Neptune obtained by the Voyager 2 spacecraft have shown clear evidence of two distinct classes of radiation characterized as smooth and bursty. At Uranus, the smooth emission is seen as broadband continuous emissions, from a few kilohertz to about 900 kHz and continuous in time over periods of a few hours. Many studies have suggested the b–smooth emission is generated by the cyclotron–maser instability [e.g. Kaiser et al., 1987; Menietti et al., 1990]. The Uranian broadband bursty (b–bursty) emission is seen in the range from 300–700

Department of Space Sciences, Southwest Research Institute, San Antonio, TX 78228–0510

kHz and occurs at times which are intermediate between the observations of the smooth emissions (see Plate 1 of Farrell and Calvert [1989] for an excellent graphical display). Thus, the smooth and bursty emissions are quite distinct in frequency range, duration and spacecraft event time.

Many early studies based on straight-line propagation [cf. Leblanc et al., 1987 and Farrell and Calvert, 1989] indicated the source of the b-bursty emission was co-located with the smooth emission near the south magnetic pole. These early studies generally agree that the emission propagates at large wave normal angles and suggest the cyclotron maser instability (CMI) as the source mechanism. However, Curran et al. [1990] have shown, via a ray tracing study, that refractive effects are important and that the source of the bursty emissions appears to be at lower latitudes for emission initially propagating at large wave normal angles. The conclusion of this latter study was that since the source region is different from that of the b-smooth emission, it is possible that the emission may be due to a distinct plasma distribution at lower latitudes or a source mechanism that is different from that which generates the b-smooth emission.

Observations of the radio emission obtained by the Voyager 2 flyby of Neptune also show clear examples of both a bursty and a smooth component [e.g. Warwick et al., 1989; Farrell et al., 1990]. The bursty emission is observed between 500 kHz and 1.3 MHz while the smooth emission is seen in the frequency range $f < 500$ kHz. The bursty emission is also generally observed at distinct times from the smooth emission and their source regions appear to be different [Farrell et al., 1990; Ladreiter et al., 1991]. The emission appears to occur in episodes with strong bursts of duration < 6 seconds, and the polarization is consistent with the right-hand extraordinary mode. Generally the bandwidth of the Neptune bursty emission is much shorter than the b-bursty emission at Uranus, with the former having a bandwidth of less than 20 kHz.

It has been suggested that both the smooth and bursty emissions are due to the electron cyclotron emissions, similar to the proposal for the emissions at Uranus [e.g., Farrell et al., 1990 and references therein]. However, the above differences in the characteristics of the smooth and bursty emissions suggest that either there are distinct emission mechanisms at work and/or that there are distinct differences in the plasma conditions in the source region.

Recently Wong and Goldstein [1990] suggested a new mechanism for producing bursty radio emission under conditions expected in planetary magnetospheres using temperature anisotropic electron beams. This mechanism was originally proposed by Goldman and Newman [1987] to explain a 'new electromagnetic beam mode' discovered in laboratory experiments reported by Urrutia and Stenzel [1984]. The mechanism suggests that a gyrating electron beam or an electron beam with a temperature anisotropy of the form $T_\perp \gg T_\parallel$ can directly generate EM radiation through a cyclotron resonant-wave-particle interaction. Newman et al. [1988] subsequently performed a comprehensive study of the mechanism including numerical simulations for the case when the ratio of the plasma frequency (ω_{pe}) to gyrofrequency (Ω_e) was greater than 2. Wong and Goldstein [1990] have extended the theory to the region of $\omega_{pe}/\Omega_e \lesssim 1$ typical of planetary magnetospheres. Their results suggest that this mechanism, hereafter called the electromagnetic beam instability (EBI), can easily generate radiation as much as a factor of two above the

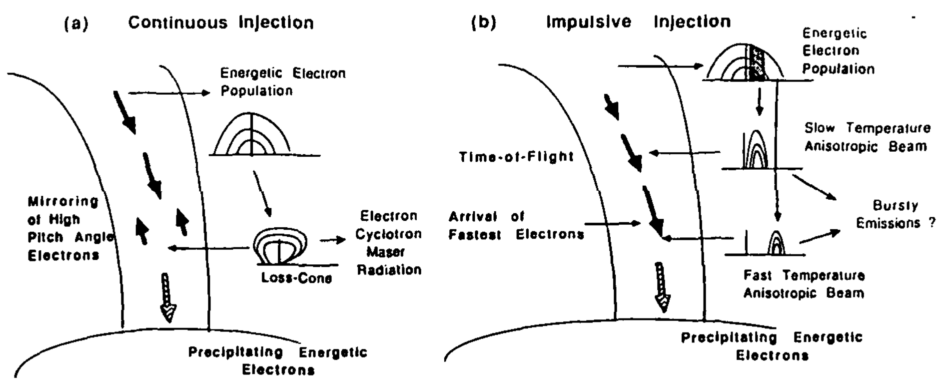

Figure 1: Schematic showing (a) the development of a loss-cone distribution during continuous injection of energetic electrons and the subsequent generation of maser emission responsible for the smooth emissions and (b) the development of a temperature anisotropic beam during impulsive injection. This type of beam can drive a modified Weibel instability which can generate radiation which can possibly account for the bursty emissions.

electron cyclotron frequency, the radiation being beamed into a filled emission cone of half-angle less than 30°.

In this paper one-dimensional particle-in-cell simulations are used to investigate the radiation from electron beams with a large temperature anisotropy. It is shown that these beams, which would typically orginate from the sporadic or impulsive injection of energetic electrons, can generate electromagnetic radiation which should be able to escape into the solar wind when the ratio of the electron plasma frequency ω_{pe} to the electron cyclotron frequency Ω_e is between about 0.4 to 1.0. Moreover, this parameter regime complements that required for the maser instability which tends to be restricted to $\omega_{pe}/\Omega_e \lesssim 0.3$ and thereby provides a natural explanation for the apparent differences in source location and spacecraft event times between the smooth and bursty emissions.

2 Comparison between maser and beam instabilities

The processes which may be involved in the generation of both the smooth and bursty emissions are illustrated in Figure 1. The standard model for producing the smooth emissions is shown in Figure 1a. Because of the long duration of the smooth emissions, there must be a continual resupply of the energetic electrons producing the radiation otherwise the driving mechanism would quickly saturate and the emissions would cease. For such a continual flow of energetic electrons down the field lines, a loss cone distribution would form, as electrons with high pitch angles mirror and move back up the field lines, while electrons with small pitch angles precipitate out of the flux tube and are lost to the lower atmosphere. Such loss-cone distributions are unstable to the maser instability which generates the observed radiation for the smooth emissions.

For the bursty emissions, the physics involved is substantially different. In particular, the presence of short bursts implies that the energetic electrons responsible for the emissions are being injected intermittently. For rapid or impulsive injection, only certain particles can reach a point further down the field line at any particular time, since slow particles would not have had sufficient time to reach it and fast particles would have already passed by [e.g., White et al., 1986; Winglee and Dulk, 1986]. As a result of these time-of-flight effects, the distribution locally can be narrowly confined in the parallel velocity, allowing the distribution to develop a beam-like feature. Furthermore, since the time-of-flight effects depend only weakly on the perpendicular velocity (assuming only weak magnetic field convergence), the particles arriving at any particular point can have a much larger spread in the perpendicular velocity than in their parallel velocity, effectively giving the beam a temperature anisotropy as well. Note that these types of distributions can develop from the same initial distribution as that driving the loss-cone formation; the main differences in the evolution of the distribution arise from the duration over which the particles are injected.

These temperature anisotropic beams are unstable to a modified kinetic 'Weibel instability' or electromagnetic beam instability [Newman et al., 1988]. When the ratio of the plasma frequency ω_{pe} to the electron cyclotron frequency Ω_e is much greater than one, modified whistlers are excited [Newman et al., 1988]. However, if $\omega_{pe}/\Omega_e < 1$, then Wong and Goldstein [1990] predict that the dominant emission is in the RCP X-mode with $\omega > \Omega_e$ and it is this radiation which they propose as the possible source of the bursty planetary emissions. In the following, the non-linear evolution of the instability is examined through particle simulations in order to compare the characteristics of the radiation with that from the maser instability and, thereby, provide better insight into the possible origins of the bursty and smooth emissions.

3 Particle distributions and particle heating

The non-linear evolution of the electromagnetic beam instability is investigated via one-dimensional (three velocity) electromagnetic particle simulations [cf. Newman et al., 1988]. This code solves self-consistently the full set of Maxwell's equations and allows the evaluation of the competition between electromagnetic and electrostatic beam instabilities. The system is assumed to be periodic with the wavevector k directed along the magnetic field which is in the X-direction. The size of the system L is assumed to be 1024 Debye lengths and the corresponding wavenumber of a mode m in the system is then $2\pi m/L$.

In all the following simulations the density of the plasma is kept constant and the magnetic field strength is varied so that ω_{pe}/Ω_e ranges from a maximum value of 2.5 down to a minimum value of 0.4. This parameter regime extends that considered by Newman et al. [1988] where only values of $\omega_{pe}/\Omega_e \geq 2.5$ were considered.

The plasma is assumed to consist of (i) a cold ambient plasma with a Maxwellian distribution with thermal speed v_{Tc} equal to $0.04c$ and which comprises 90% of the total electron density and (ii) a beam component with a beam speed v_b equal to $4v_{Tc}$, a parallel temperature the same as the cold component and a perpendicular temperature 36 times

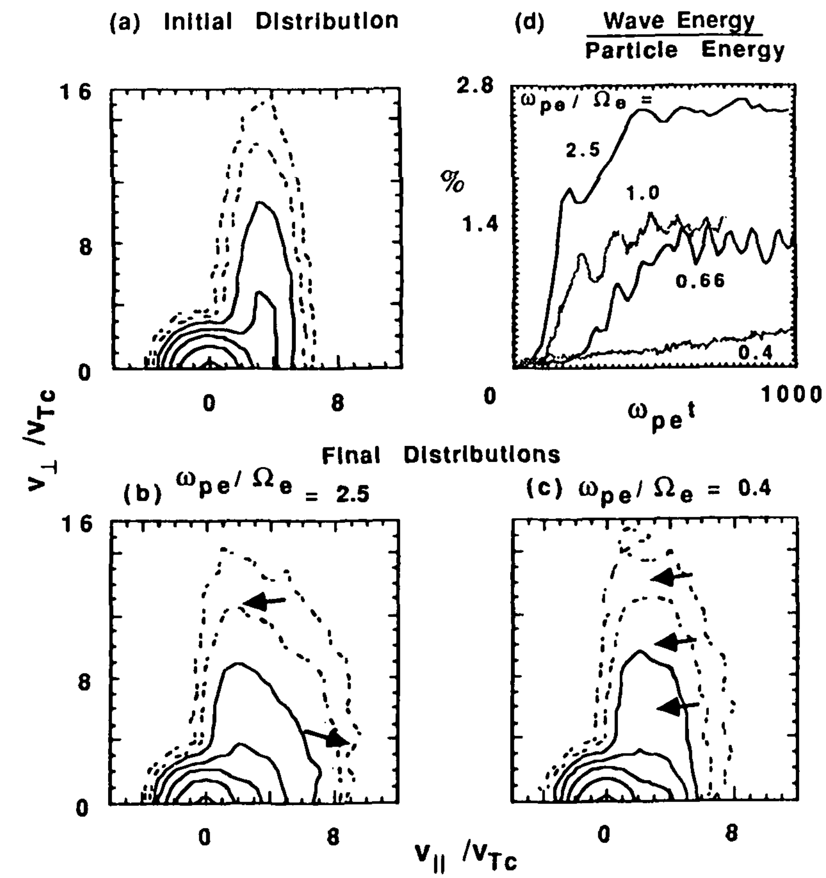

Figure 2: Evolution of the total electron distribution. The initial distribution is shown in (a) and the final distributions at saturation are shown in (b) and (c) for ω_{pe}/Ω_e equal to 2.5 and 0.4, respectively. The time history of the percentage of the particle energy converted to wave energy is shown in (d).

the parallel temperature, i.e $v_{T\parallel E} = v_{Tc}, v_{T\perp E} = 6v_{T\parallel E}$. These parameters are similar to those used by Newman et al. [1988].

The initial distribution comprising these two components is shown in Figure 2a. It is unstable to both the electromagnetic beam instability as well as a weak electrostatic beam instability (similar to the normal bump-in-tail instability). The electrostatic instability quickly saturates (by $\omega_{pe}t \simeq 100$) and produces only some flattening of the distribution between $3 \lesssim v_\parallel/v_{Tc} \lesssim 4$. Most of the particle heating is driven by the electromagnetic beam instability, as illustrated in Figures 2b and c which show the velocity distributions at saturation ($\omega_{pe}t \simeq 1000$) for the extreme values of ω_{pe}/Ω_e considered.

For $\omega_{pe}/\Omega_e \gtrsim 1$ (Figure 2b), the electromagnetic beam instability scatters low pitch angle electrons forward to higher $v_{\parallel}$ and high pitch angle electrons to lower pitch angles and lower energies. For $\omega_{pe}/\Omega_e \lesssim 1$, the beam particles experience primarily only scattering to lower pitch angles and energies. The fraction of particle energy converted to wave energy is shown in Figure 2d. The efficiency is seen to increase with increasing ω_{pe}/Ω_e even though the instability at high ω_{pe}/Ω_e is associated with acceleration of some of the particles to higher $v_{\parallel}$. This increase in efficiency is consistent with the increase in the expected growth rate of the instability as ω_{pe}/Ω_e is increased for a fixed energetic component [cf. Wong and Goldstein, 1990]. It should also be noted that the efficiency of the instability is comparable to that of the maser instability [e.g., Pritchett, 1986], i.e. the electromagnetic beam instability can, under certain conditions, produce radiation as intense as the maser instability.

4 Characteristics of the wave spectrum

The characteristics of the excited waves are expected to change as ω_{pe}/Ω_e is varied from above to below unity. In particular, for $\omega_{pe}/\Omega_e \gtrsim 1$ the whistler, through a Doppler shift associated with the presence of the beam, can have a frequency comparable to the electron cyclotron frequency, allowing gyro-resonant interactions to occur. However, when $\omega_{pe}/\Omega_e \lesssim 1$, the maximum frequency of the whistler is limited to ω_{pe} where it becomes increasingly electrostatic so that gyroresonant interactions are suppressed. However, the cutoff for the X-mode and resonance for the Z-mode start to approach the cyclotron frequency and it is these modes which can then become unstable through gyro-resonant interactions.

This change in the mode structure is illustrated in Figure 3 which shows the spectrum derived from integrating the power in the different k modes over the full period of the simulations. It is seen that, for $\omega_{pe}/\Omega_e = 2.5$, the dominant emission is at about 0.5 Ω_e and is left hand polarized (LCP). This mode is essentially a beam-modified backward propagating whistler. Because its frequency is below Ω_e this emission is expected to be trapped in a planetary magnetosphere.

At the intermediate values of ω_{pe}/Ω_e (Figures 3b and c), there is still relatively strong emission at 0.5 Ω_e. In addition, strong emissions at frequencies slightly above Ω_e appear. This is the RCP X-mode predicted by Wong and Goldstein [1990] and it is this radiation, particularly for the lower values of ω_{pe}/Ω_e, which can escape into the solar wind and produce the bursty emissions. Since this is the only component that can escape, the observed radiation should be highly polarized similar to the radiation from the maser instability. At still lower values of ω_{pe}/Ω_e (Figures 3d), the LCP emission is essentially suppressed and the emission in the RCP Z-mode at frequencies fractionally below the Ω_e becomes increasingly stronger.

In addition to the above variations in the overall spectrum of the generated radiation, there are also significant changes in the temporal evolution of the dominant modes as ω_{pe}/Ω_e is varied. As an example, Figure 4 shows the time histories of the power of the dominant modes for ω_{pe}/Ω_e equal to (i) 1.0 and (ii) 0.4. For the higher value of ω_{pe}/Ω_e the modes grow approximately monotonically up to their peak value and then stay approximately

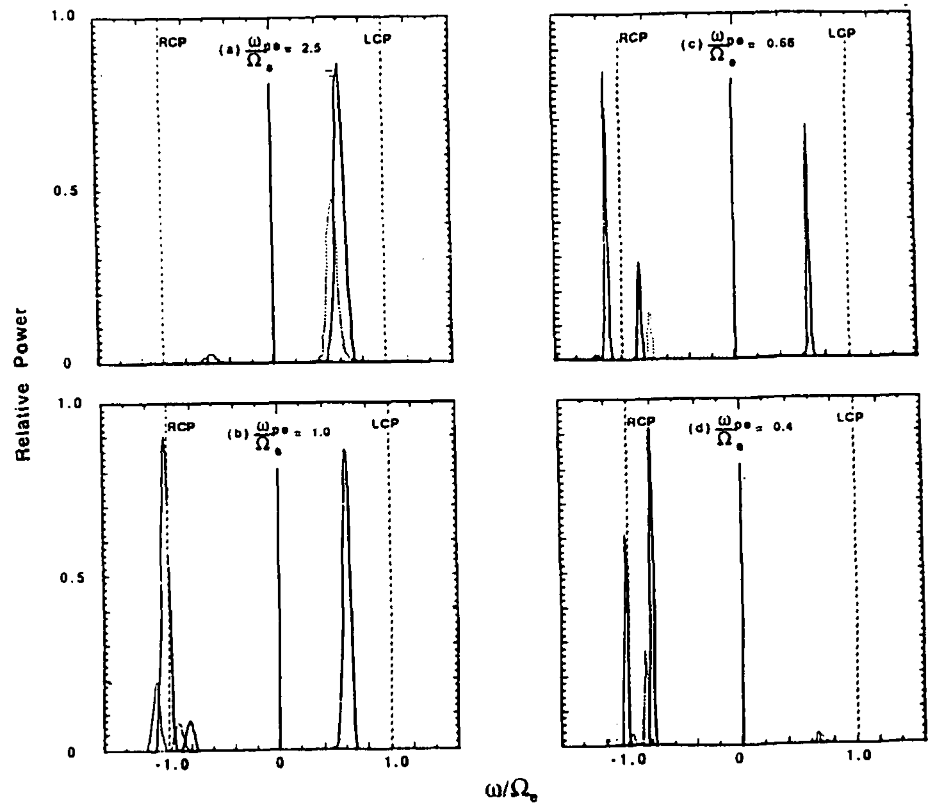

Figure 3: Power spectra of the dominant modes for the cases shown in Figure 3. The spectra have been normalized so that the spectral peak has approximately the same value in each case. For the highest value of ω_{pe}/Ω_e, the LCP mode with $\omega \simeq 0.5\Omega_e$ dominates but as ω_{pe}/Ω_e is decreased the RCP modes dominate, with intense emissions above Ω_e being generated.

constant, with possibly a small, slow decay. This type of temporal evolution is similar to that of the maser instability and would be probably more closely associated with long duration bursts.

For the smaller value of ω_{pe}/Ω_e (right hand side of Figure 4), the temporal evolution of the dominant mode is significantly different. Instead of a monotonic rise, the amplitude of the modes is seen to reach a series of local maxima. These temporal variations are due to the competition between the modes for the available free energy. In particular, the maxima and minima of the two modes shown are approximately anti-correlated. As a result of this competition, the radiation in this parameter regime is intrinsically bursty.

The growth rates for the different modes can be directly calculated from the time histories shown in Figure 4. For $\omega_{pe}/\Omega_e = 1.0$ (Figure 4a), the growth rate of the LCP mode is

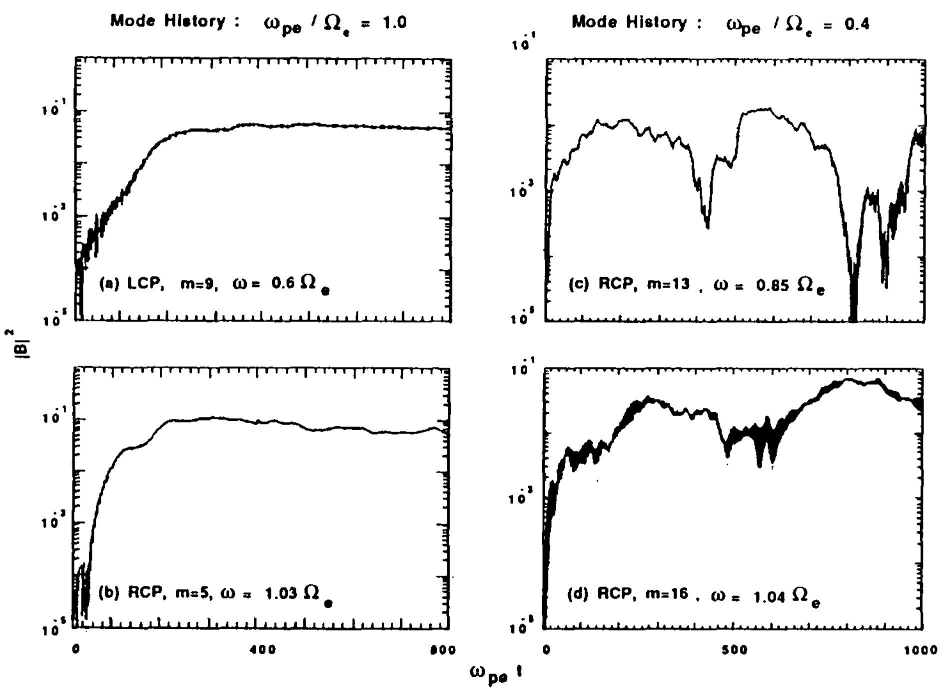

Figure 4: Time histories of the power in dominant modes for ω_{pe}/Ω_e equal to 1.0 (left hand side) and 0.4 (right hand side). At the lower value of ω_{pe}/Ω_e, the emissions are bursty due to competition modes.

about 0.02 Ω_e and between about 0.02 and 0.04 Ω_e for the RCP mode. For $\omega_{pe}/\Omega_e = 0.4$, the growth rate is smaller being about 2–4$\times 10^{-3}$ Ω_e. These growth rates are consistent with the linear growth rates predicted by Wong and Goldstein [1990] and are comparable to those for the maser instability.

5 Conclusions

One–dimensional electromagnetic particle simulations have been used to evaluate the characteristics of radiation from electron beams with temperature anisotropies in order to identify the origin of bursty planetary emissions. Such beams can arise for example during the impulsive injection of energetic electrons with time–of–flight effects restricting the parallel velocity of the particles arriving at any particular point down the field lines at a specific time. Observations of temperature anisotropies and electron beams in the Earth's auroral region have recently been reported for terrestrial observations [cf. Menietti and Burch, 1991]. These observations indicate that temperature anisotropies ($T_\perp \gg T_\parallel$) exist adjacent to source regions of the cyclotron maser emission. In contrast, the smooth

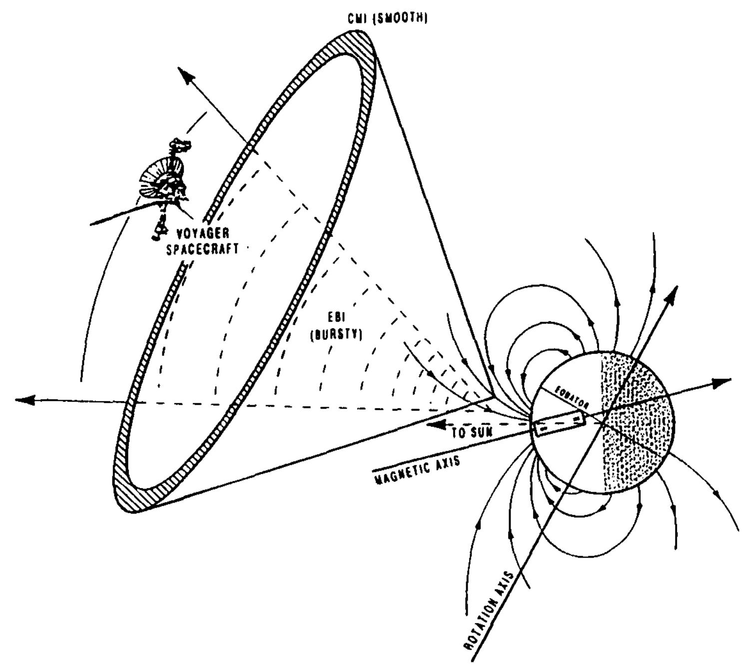

Figure 5: Schematic showing the radiation pattern in the proposed model. Radiation from the cyclotron maser emission (CMI) in a hollow cone generates the smooth emissions while the electromagnetic beam instability (EBI) generates radiation in a displaced solid cone to produce the bursty emissions.

planetary emissions are believed to be generated by the cyclotron maser instability (CMI) which is presumably driven by the continuous injection of the energetic electrons and the subsequent development of loss–cone distributions.

These temperature anisotropic beams are unstable to a modified kinetic Weibel or electromagnetic beam instability. For $\omega_{pe}/\Omega_e \gtrsim 1$, most of the wave energy generated is LCP with frequencies below the cyclotron frequency and is therefore trapped. However, for $\omega_{pe}/\Omega_e \lesssim 1$ the dominant mode is RCP and freely propagating. The radiation in this regime is also bursty in nature due to the competition between different modes, particularly for small values of ω_{pe}/Ω_e. In addition, the electromagnetic beam instability is as efficient as the maser instability in converting particle energy into wave energy particularly when $\omega_{pe}/\Omega_e \gtrsim 0.4$.

Thus, the radiation from the electromagnetic beam instability (EBI) has many features similar to the observed bursty planetary emissions. Moreover, it strongly complements that of the maser radiation, both in the plasma conditions in which escaping radiation is generated and in the injection of the energetic electrons as it changes from continuous to sporadic. This complementary nature provides a ready explanation for the apparent offsets in source location and spacecraft event time of the smooth and bursty emissions. In addition, Curran et al. [1990] have shown via a ray tracing study that for $\omega_{pe}/\Omega_e \lesssim 0.25$ and emission radiated in hollow cones at large wave normal angles, the source of Uranus broadband bursty emission is distinct from the b–smooth emission. No ray tracing studies of filled emission cones have yet been reported for either Uranus or Neptune.

The model presented here suggests a radiation pattern and source location similar to that shown in Figure 5, with the source regions of the two emissions approximately adjacent, as ω_{pe}/Ω_e and the characteristics of the electron injection vary across the polar regions. As a result of the different emission mechanisms and there source location, a spacecraft would be expected to see the two sides of the hollow cone of the smooth emissions followed by a single patch of bursty emission associated with emission from a filled cone, similar to the observations of Farrell and Calvert [1989].

While the above work provides a proof–in–principle of the importance of the EBI, more work needs to be carried out to fully determine the radiation pattern from the electromagnetic beam instability and its propagation through the magnetospheres of Neptune and Uranus.

Acknowledgements: This research was supported by NASA grants NAGW-2471, NAGW-2412 and NAGW-1936 and NSF grant ATM 91-96132 to Southwest Research Institute and by SWRI Internal Research grants 15-9668 and 15-9677. The simulations were performed on the CRAY Y-MP at the San Diego Supercomputing Center which is funded by the National Science Foundation.

References

Curran, D. B., J. D. Menietti, and H. K. Wong, Ray tracing of broadband bursty radio emissions from Uranus, *Geophys. Res. Lett.*, **17**, 109, 1990.

Farrell, W. M. and W. Calvert, The source location and beaming of broadband bursty radio emissions from Uranus, *J. Geophys. Res.*, **94**, 217, 1989.

Farrell, W. M., M. D. Desch, and M. L. Kaiser, Field–independent source localization of Neptune's radio bursts, *J. Geophys. Res.*, **95**, 19143, 1990.

Goldman, M. V. and D. Newman, Electromagnetic beam modes driven by anisotropic electron streams, *Phys. Rev. Lett.*, **58**, 1849, 1987.

Kaiser, M. L., M. D. Desch, and S. A. Curtis, The sources of Uranus' dominant nightside radio emissions, *J. Geophys. Res.*, **92**, 15169, 1987.

Ladreiter, H. P, Y. Leblanc, G. Rabl and H. O. Rucker, Emission characteristics and source location of smooth Neptunian kilometric radiation, *J. Geophys. Res.*, **96**, 19101, 1991.

Leblanc, Y., M. G. Aubier, A. Ortega–Molina, and A. Lecacheux, Overview of the Uranian radio emissions: Polarization and constraints on source locations, *J. Geophys. Res.*, **92**, 15125, 1987.

Menietti, J. D., H. K. Wong, D. A. Wah, and C. S. Lin, Source region of the smooth high frequency nightside Uranus kilometric radiation, J. Geophys. Res., **95**, 51, 1990.

Menietti, J. D. and J. L. Burch, Particle acceleration in the auroral region as observed by DE–1, Proc. AGU Chapman Conference on Auroral Plasma Dynamics, October 21–25, 1991 in Minneapolis, MN.

Newman, D., R. M. Winglee, and M. V. Goldman, Theory and simulation of electromagnetic beam modes and whistlers, *Phys. Fluids*, **31**, 1515, 1988.

Pritchett, P. L., Electron–cyclotron maser instability in relativistic plasmas, *Phys. Fluids*, **29**, 2919, 1986.

Urrutia, J. M. and R. L. Stenzel, New electromagnetic mode in a non–Maxwellian high–beta plasma, *Phys. Rev. Lett.*, **53**, 1901, 1984.

Warwick, J. W., D. R. Evans, G. R. Peltzer, R. G. Peltzer, J. H. Romig, C. B. Sawyer, A. C. Riddle, A. E. Schweitzer, M. D. Desch, M. L. Kaiser, W. M. Farrell, T. D. Carr, I. de Pater, D. H. Staelin, S. Gulkis, R. L. Poyntner, A. Boischot, F. Genova, Y. Leblanc, A. Lecacheux, B. M. Pedersen, P. Zarka, Voyager planetary radio astronomy at Neptune, *Science*, **246**, 1498, 1989.

White, S. M., D. B. Melrose and G. A. Dulk, Electron cyclotron masers during solar flares, *Astrophys. J.*, **308**, 424, 1986.

Winglee, R. M. and G. A. Dulk, The electron–cyclotron maser instability as the source of solar type V continuum, *Astrophys. J.*, **310**, 432, 1986.

Wong, H. K. and M. L. Goldstein, A mechanism for bursty radio emission in planetary magnetospheres, *J. Geophys. Res.*, **17**, 2229, 1990.

JOURNAL OF GEOPHYSICAL RESEARCH, VOL. 99, NO. A1, PAGES 235–239, JANUARY 1, 1994

N15

Electron cyclotron wave generation by relativistic electrons

H. K. Wong
Department of Space Sciences, Southwest Research Institute, San Antonio, Texas

M. L. Goldstein
Laboratory of Extraterrestrial Physics, NASA Goddard Space Flight Center, Greenbelt, Maryland

Abstract. We show that an energetic electron distribution which has a temperature anisotropy ($T_{\perp b} > T_{\parallel b}$), or which is gyrating about a DC magnetic field, can generate electron cyclotron waves with frequencies below the electron cyclotron frequency. Relativistic effects are included in solving the dispersion equation and are shown to be quantitatively important. The basic idea of the mechanism is the coupling of the beam mode to slow waves. The unstable electron cyclotron waves are predominantly electromagnetic and right-hand polarized. For a low-density plasma in which the electron plasma frequency is less than the electron cyclotron frequency, the excited waves can have frequencies above or below the electron plasma frequency, depending upon the parameters of the energetic electron distribution. This instability may account for observed Z mode waves in the polar magnetosphere of the Earth and other planets.

Introduction

The Earth's polar magnetosphere has long been recognized as an active region of wave activities. In the last two decades, numerous spacecraft have sampled this region of space and have identified a large variety of wave modes, most notably the auroral hiss and the auroral kilometric radiation (AKR). For a review, see *Shawhan* [1979]. These waves are believed to play an important role in various plasma processes in the magnetosphere through wave-particle interactions. Examples of such processes include the diffusion of auroral electrons by electrostatic electron cyclotron waves [*Kennel and Ashour-Abdalla*, 1982], the generation of AKR through relativistic cyclotron resonance [*Gurnett*, 1974; *Wu and Lee*, 1979] and the acceleration and heating of ions and electrons by waves in the auroral region leading to the formation of ion and electron conical distributions (see, for example, *Chang et al.* [1986], *Crew et al.* [1990], *Lysak* [1986], *Temerin and Cravens* [1990], and *Wong et al.* [1988], among others).

The whistler mode has been studied extensively in the past, primarily due to the interest in VLF emissions, auroral hiss, and lightning-related phenomena. In the midaltitude polar magnetosphere, the electron plasma frequency $\omega_e = (4\pi n_e e^2/m_e)^{1/2}$ is typically less than the electron cyclotron frequency $\Omega_e = |e|B_0/m_e c$, where m_e is the electron rest mass, n_e is the electron density, B_0 is the magnitude of the ambient magnetic field, and c is the speed of light. Under this condition, the whistler mode propagates between the lower hybrid frequency, which is approximately the ion plasma frequency ω_i, and ω_e. The frequently observed whistler mode auroral hiss is believed to be generated near the resonance cone either by precipitating electrons or by upward moving electron beams [*Gurnett et al.*, 1983]. The whistler waves excited near the resonance cone are quasi-electrostatic waves with negligible magnetic components; however, analysis of the "funnel-shaped" auroral hiss observed by DE 1 indicates that the auroral hiss has a considerable magnetic component [*Gurnett et al.*, 1983]. Subsequent stability analysis using the observed particle distributions has revealed that the electron acoustic wave, rather than the whistler wave, is the dominant unstable wave driven by such electron beam distributions [*Lin et al.*, 1984, 1985; *Tokar and Gary*, 1984]. The electron acoustic wave is electrostatic in nature, and thus might account for the electrostatic component of auroral hiss; however, the origin of the electromagnetic component of the hiss still remains unanswered.

In a different context, *Benson et al.* [1988] have reported ground-based detection of waves in the frequency range 150–300 kHz, indicating the generation of field-aligned waves in the auroral zone. The field-aligned waves observed by *Benson et al.* [1988] are electromagnetic and fall into the frequency range of the whistler mode and overlap the frequency range of AKR. However, because the theories usually proposed for the generation of AKR produce radiation in the extraordinary and ordinary modes which cannot reach the ground, the field-aligned radiation observed by *Benson et al.* [1988] must be generated by a different mechanism. Motivated by these observations, *Wu et al.* [1989] showed that an energetic electron population with either a temperature anisotropy or a trapped type distribution can generate field-aligned waves in the observed frequency range. More recently, *Ziebell et al.* [1991] have generalized *Wu et al.'s* [1989] theory to investigate propagation effects on the amplification of radiation along the field line.

Previously we have studied the generation of bursty radio emission by low-density anisotropic or gyrating electron beams [*Wong and Goldstein*, 1990] (hereinafter paper 1). In

Paper number 93JA02319.
0148-0227/94/93JA-02319$05.00

the present study we extend that analysis by including relativistic effects and show that the frequency range of the unstable waves excited by dense gyrating and/or anisotropic distributions can extend below Ω_e or even below ω_e. In this regard our analysis is a generalization of the previous work by *Wu et al.* [1989] because we extend into the relativistic regime, include oblique propagation, and use a more general distribution function that includes a beam component. The process we describe appears to provide an alternative to the cyclotron maser instability for generating *Z* and *O* mode radiation.

Physical Model and Results

The physical model we consider is the same as previously discussed in paper 1: a gyrating or anisotropic electron beam in a cold background magnetized plasma. Because the frequencies we consider are close to Ω_e or ω_e, we can ignore the ion contribution to the plasma dielectric. In paper 1 we discussed the conditions under which such distributions can arise and we do not repeat that discussion here. The general form of the energetic electron distribution we use is

$$f_b(u_\parallel, u_\perp) = \frac{A}{\pi^{3/2}\alpha_{\perp b}{}^2 \alpha_{\parallel b}} \exp\left[-\frac{(u_\perp - u_{\perp 0})^2}{\alpha_{\perp b}{}^2} - \frac{(u_\parallel - u_b)^2}{\alpha_{\parallel b}{}^2}\right] \quad (1)$$

where $\mathbf{u} = \mathbf{p}/m_e$ is the momentum per unit mass, $\alpha_{\perp,\parallel b} = (2\kappa T_{\perp,\parallel b}/m_e)^{1/2}$, κ is Boltzmann's constant, u_b and $u_{\perp 0}$ are the momenta per unit mass of the electron beam parallel and perpendicular to the magnetic field, respectively, and the normalization constant is found from $A^{-1} = \exp(-u_{\perp 0}^2/\alpha_{\perp b}^2)[1 - i(u_{\perp 0}/\alpha_{\perp b})\, Z(i(u_{\perp 0}/\alpha_{\perp b})]$ to ensure that $\int d^3u f_b(\mathbf{u}) = 1$.

A general derivation of the relativistic electromagnetic dispersion equation for arbitrary directions of propagation can be found in the work by *Baldwin et al.* [1969]. In the appendix we give a brief description of how we solve the dispersion equation numerically. Most of the discussion below will be limited to parallel propagating solutions, primarily because the maximum growth is generally at 0°. However, we have also solved the more general obliquely propagating relativistic dispersion equation, and we discuss below some of those results (Figure 6).

For comparison purposes, we first show solutions to the nonrelativistic dispersion equation for parallel propagating modes excited by trapped electrons with energies of the order of several keV, a case discussed previously by *Wu et al.* [1989]. The dispersion relation was solved using $n_b = 0.9$, $n_e = 9n_c$, where n_b and n_c are the densities of the energetic and background electrons, respectively; and $n_e = n_b + n_c$. Note that, in contrast to paper 1, we emphasize here a regime in which the density of the energetic electron component, n_b, exceeds that of the background, n_c. We used five values of ω_e/Ω_e, viz. 0.1, 0.2, 0.4, 0.6, and 0.8. In the example shown in Figure 1, the drift of the electrons is zero, and the parallel and perpendicular temperatures of the energetic electrons are both 2.5 keV. The ring speed is $u_{\perp 0} = 2.0$ in units of $\alpha_{\perp b}$. In Figure 1 we plot the real and imaginary frequencies (ω_r and ω_i, respectively) as functions of wave number. The frequencies are normalized by Ω_e, and the wave numbers by Ω_e/c. Note that ω_r and ω_i are plotted on linear and logarithmic scales, respectively. One should keep in mind in these analyses that because the growth rates are functions of ω_e/Ω_e and n_b/n_e, specific values of density need not be specified.

As is evident from Figure 1, the instability exists for the entire range of the values of ω_e/Ω_e considered, as does the bandwidth of the instability. For small values of ω_e/Ω_e, the frequency of the unstable waves lies between ω_e and Ω_e, which is in the frequency regime of the *Z* and *O* modes. For larger values of ω_e/Ω_e, the frequency of the unstable waves can extend below ω_e; the waves are then in the whistler and *Z* mode branches for frequencies above the left-hand cutoff. This result is essentially the same as was found by *Wu et al.* [1989], as can be verified by comparing our Figure 1 with their Figure 3.

In Figure 2 we show the effect on the magnitude of the growth rates when using the relativistic dispersion relation. The parameters are the same as we used in Figure 1, except that now $\omega_e/\Omega_e = 0.8$. It is clear that both the bandwidth and magnitude of the instability are reduced. The reduction in bandwidth is from $\Delta kc/\Omega_e \cong 0.6$ to $\Delta kc/\Omega_e \cong 0.4$, while the maximum growth rate drops by nearly a factor of 5. Thus it is clear that relativistic effects can be quantitatively important in this class of instabilities. For the remainder of this paper, all results will be computed using the relativistic dispersion equation.

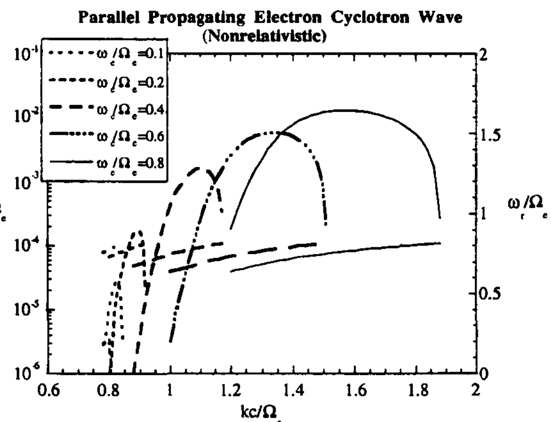

Figure 1. The unstable roots of the nonrelativistic dispersion equation plotted for comparison with Figure 3 of *Wu et al.* [1989]. The distribution function of the energetic electrons, given by (1), is normalized so that $n_b = 0.9$ and $n_e = 9n_c$. The parallel and perpendicular temperatures of the energetic electrons both equal 2.5 keV, and the ring speed is $u_{\perp 0}/\alpha_{\perp b} = 2.0$ (the beam speed $u_\parallel = 0$). The real and imaginary parts of ω are plotted on linear and logarithmic scales, respectively, for ω_e/Ω_e = 0.1, 0.2, 0.4, 0.6, and 0.8. Frequencies are normalized by Ω_e and wave numbers by Ω_e/c.

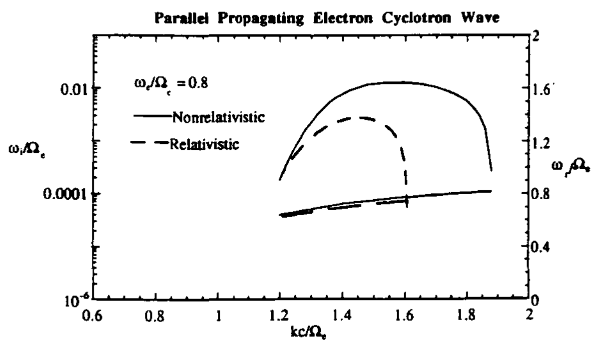

Figure 2. Comparison between solutions of the relativistic and nonrelativistic dispersion equations for the same parameters are were used in Figure 1 except that only the results for $\omega_e/\Omega_e = 0.8$ are shown.

For zero drift speed ($u_{\perp 0} = u_b = 0$), this instability can also be driven by a temperature anisotropy, as is illustrated in Figure 3. Here the density ratio between the energetic and background electron distributions remains as before, $\omega_e/\Omega_e = 0.6$, and the parallel temperature of the energetic electrons is kept constant at 2.5 keV, while the perpendicular temperature is increased from $T_{\perp b}/T_{\parallel b} = 4$ to $T_{\perp b}/T_{\parallel b} = 10$. For $T_{\perp b}/T_{\parallel b} = 4$ the growth rate is very small ($\omega_{i,max}/\Omega_e \cong 10^{-4}$), but it increases by more than 2 orders of magnitude as the anisotropy increases to $T_{\perp b}/T_{\parallel b} = 10$. Clearly, at $T_{\perp b}/T_{\parallel b} = 4$ the instability is near threshold (note the rapid increase from $T_{\perp b}/T_{\parallel b} = 4$ to $T_{\perp b}/T_{\parallel b} = 5$) — subsequent increases in $T_{\perp b}/T_{\parallel b}$ produce far smaller changes in the maximum rate of growth.

Figure 4 illustrates the behavior of the instability as the ring speed is varied from $u_{\perp 0}/\alpha_{\perp b} = 2.8$ to 3.2. The parameters used in these calculations are again the same as above, except that $\omega_e/\Omega_e = 0.4$. The growth rate is a fairly sensitive function of $u_{\perp 0}/\alpha_{\perp b}$, which can be understood because the free energy of the ring is equivalent to a temperature anisotropy, as discussed by *Wong and Goldstein* [1987]. Recall from Figure 2 that relativistic effects can significantly reduce the growth rate from the values calculated nonrelativistically, especially for relatively small values of ω_e/Ω_e and/or $u_{\perp 0}$. This must be kept in mind when comparing Figures 2 and 4 with the nonrelativistic calculation shown in Figure 1.

In Figure 5 we investigate how finite beam speed affects the instability as $u_b/\alpha_{\parallel b}$ is varied from 0 to 2. The parameters used are again as in Figure 1, except that $u_{\perp 0}/\alpha_{\perp b} = 2.5$ and $\omega_e/\Omega_e = 0.6$. Small increases in $u_b/\alpha_{\parallel b}$ (from 0 to 1) cause the instability to broaden in bandwidth and to increase slightly in maximum growth. Further increase in $u_b/\alpha_{\parallel b}$ to 2 produces a reduction in growth and in bandwidth from what it was at $u_b/\alpha_{\parallel b} = 1$; however, it is still significantly broader than it was initially when $u_b/\alpha_{\parallel b} = 0$. This behavior contrasts sharply from the beam-driven radio emission discussed in paper 1 (cf. Figure 2 in that paper) in which the growth rate increased monotonically with increasing beam speed.

We have also investigated the behavior of this instability for oblique propagation. Again we take the thermal energy of the energetic electrons to be 2.5 keV, the density ratio of the energetic and cold components of the electron distribution equal to 9, the ring speed $u_{\perp 0}/\alpha_{\perp b} = 2.5$, and $\omega_e/\Omega_e = 0.6$. The distribution has no drift ($u_b = 0$). The real and imaginary parts of ω are plotted in Figure 6 as a function of θ, the angle between **k** and **B**. The plot is constructed at the wave number of maximum growth of the instability at $\theta = 0°$, $kc/\Omega_e = 1.28$. For this wave number, the instability extends to approximately 10°, and then drops rapidly to zero. This does not necessarily mean, however, that there is no instability at larger angles. For the parameters of this example, as the propagation angle changes, the wave number of local maximum growth at that value of θ shifts to lower values of k, and the cone of unstable wave vectors extends somewhat beyond 15°. Nonetheless, the instability still grows most rapidly at $\theta = 0°$. There is little Landau damping at these frequencies, and these oblique waves are primarily electromagnetic in nature.

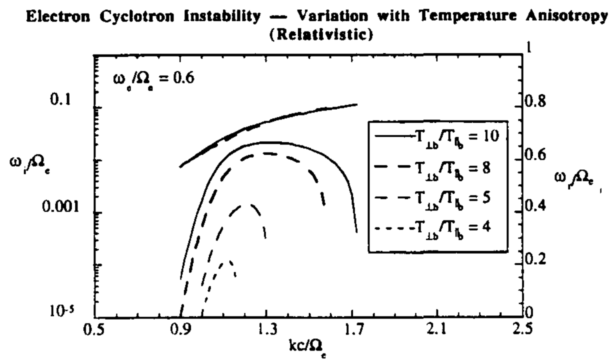

Figure 3. Variation in the growth rate of the electron cyclotron instability with changes in temperature anisotropy. The beam speed is 0, and $\omega_e/\Omega_e = 0.6$. The temperature anisotropy varies from $T_{\perp b}/T_{\parallel b} = 4$ to $T_{\perp b}/T_{\parallel b} = 10$. At $T_{\perp b}/T_{\parallel b} = 4$ the instability is near threshold.

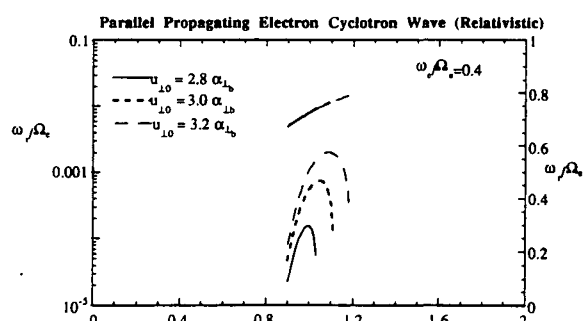

Figure 4. Variation in the growth rate of the instability for $\omega_e/\Omega_e = 0.4$ as the ring speed is varied from $u_{\perp 0}/\alpha_{\perp b} = 2.8$ to 3.2. All other parameters are the same as were used in Figure 1.

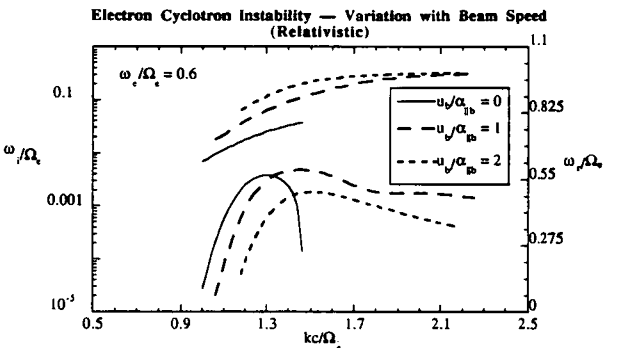

Figure 5. The effect of finite beam speed on the instability. In this case, $u_b/\alpha_{\parallel b}$ is varied from 0 to 2; $u_{\perp 0}/\alpha_{\perp b} = 2.5$, and $\omega_e/\Omega_e = 0.6$. All other parameters are the same as were used in Figure 1.

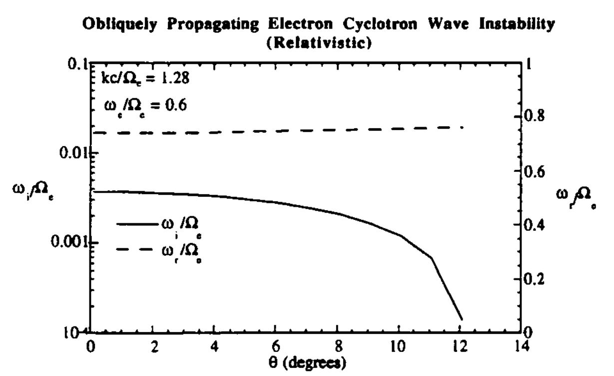

Figure 6. The behavior of the instability for off-angle propagation. The thermal energy is again 2.5 keV, $u_{\perp 0}/\alpha_{\perp b} = 2.5$, and $\omega_e/\Omega_e = 0.6$. The beam drift speed $u_{\parallel b} = 0$, and $kc/\Omega_e = 1.28$. The density of the beam is the same as was used in all figures above.

As the value of ω_e/Ω_e increases, e.g., $\omega_e/\Omega_e = 0.8$, the situation changes significantly. For large values of ω_e/Ω_e, maximum growth occurs at oblique propagation and at larger values of k than for the local maximum at $\theta = 0°$. We suspect that this change in the nature of the solution arises from the fact that the real part of the wave frequency is above the electron plasma frequency when the ratio ω_e/Ω_e is small, whereas when $\omega_e/\Omega_e = 0.8$, the excited wave has a frequency below ω_e (*cf.* Figure 1). Thus at large values of ω_e/Ω_e, the excited wave can be in the Z and whistler modes, while for small values of ω_e/Ω_e, the wave can only propagate in the Z and O modes (for a discussion of which wave modes exist at particular frequencies in the auroral region, see Figure 5 of *Gurnett et al.* [1983]). This behavior of the instability with changing ω_e/Ω_e suggests that the trapped (or ring) distribution is an effective population for generating whistler waves if the physical parameters are appropriate.

Discussion

The fundamental result of this calculation is the demonstration that a temperature anisotropy or a ring-beam electron distribution can generate electron cyclotron waves with frequencies that extend from below to above ω_e, but still below Ω_e for an underdense plasma. The calculation is relativistic and allows for arbitrary direction of propagation. Previous work [*Wu et al.*, 1989] was confined to parallel propagation and was a nonrelativistic calculation. Our result for parallel propagation agrees qualitatively with Wu et al.'s results; however, as shown in Figure 2, the effect of the relativistic corrections to the dispersion equation is to reduce substantially both the magnitude of the growth rate and the bandwidth of the unstable waves.

We also investigated the effect that finite beam speed has on the instability, an effect not considered previously. For small beam speeds, the growth rates can be enhanced and the bandwidths broadened. But as the beam speed increases, the growth rate decreases (cf. Figure 5). In paper 1 we studied the generation of bursty radio emission and showed that in plasma regimes in which $\omega_e/\Omega_e < 1$, anisotropic electron beams, or gyrating electron beams, can excite directly right-hand polarized broadband electromagnetic radiation in the X mode. The present analysis extends that work to waves with frequencies below Ω_e and also includes relativistic effects in the dispersion equation. In addition, the mechanism described in paper 1 generated unstable X mode waves when the electron distributions had large drift speeds. In contrast, for the parameters used here, the present mechanism is suppressed for large electron drift speeds and excites waves primarily in the Z or O mode. Nonetheless, the free energy source in both situations is the temperature anisotropy or ring component of the energetic electrons (the present mechanism operates even in the absence of any drift).

Recently, *Winglee et al.* [1992] have performed a one-dimensional (with three components of velocity), relativistic electromagnetic particle simulation that showed that an anisotropic electron distribution can generate freely propagating right-hand circularly polarized electromagnetic radiation if the beam speed is sufficiently large—in agreement with the results of paper 1. Winglee et al.'s simulations are periodic, and the wave vectors are parallel to the magnetic field. Besides the freely propagating wave, *Winglee et al.* [1992] also found an instability with frequencies below Ω_e—a result consistent with the theoretical analysis here. For lower values of the beam speed they found that the dominant wave mode consisted of waves with frequencies $\omega_r < \Omega_e$, whereas for large beam speeds, the dominant mode was the freely propagating X mode, also in agreement with the results shown here and in paper 1.

The motivation for the present work was observations of Z mode radiation in the Earth's auroral zone [*Gurnett et al.*, 1983] and similar phenomena at other planets [*Gurnett et al.*, 1990; *Kurth and Gurnett*, 1991]. Although Z mode radiation can be generated by the cyclotron maser instability (see, for example, *Hewitt et al.* [1983]), ray tracing studies [*Menietti and Lin*, 1986] indicate that cyclotron maser resonance may not be the only mechanism responsible for the observed Z mode emission because the generation and subsequent refraction of the waves do not appear consistent with observations. Electron cyclotron waves generated by temperature anisotropies or ring-beam distributions can have frequencies between ω_e and Ω_e in the Z and O mode ranges. Because the waves are mostly right-hand polarized, we suspect that this mechanism mainly produces Z mode radiation. The electron cyclotron waves excited in this frequency range are predominantly field-aligned and have a much broader bandwidth in frequency than waves generated by the cyclotron maser instability. Thus the electron cyclotron wave generation mechanism discussed here may provide another, complementary, explanation for observed Z mode radiation. Because a ring-beam distribution is also capable of generating Z mode radiation via the cyclotron maser instability, determining which mechanism actually dominates in any specific situation requires detailed modeling that is beyond the scope of this paper.

Conclusions

We have examined the role of relativistic effects on the generation of electron cyclotron radiation by anisotropic energetic electrons. The anisotropies are assumed to be due to either temperature anisotropies or ring (trapped) distributions. Although our results are qualitatively in agreement with previous work [*Wu et al.*, 1989], relativistic effects tend to suppress significantly the growth rate. We have also found it possible to excite electromagnetic whistler waves with maximum growth at a substantial angle from the background field for large values of ω_e/Ω_e (~ 0.8, but still less than unity). The excitation mechanism discussed in this paper may provide an alternative explanation to the cyclotron maser instability for the generation of Z mode radiation observed in planetary magnetospheres.

As shown in paper 1 and in the simulations of *Winglee et al.* [1992], a gyrating or anisotropic electron distribution can excite a variety of waves in several different frequency ranges. In addition, the same class of distributions is also unstable to the cyclotron maser instability. Which mechanism (or wave mode) dominates will depend on the detailed form of distribution and on details of the background plasma parameters. A comprehensive comparison of the relative importance of these mechanisms will have to await more extensive analytic work coupled with two-dimensional numerical simulations, including a study of the convective properties of these instabilities along auroral field lines (for example, *Ziebell et al.* [1991]).

Appendix

In this derivation, two electron components are immersed in a uniform, external magnetic field $\mathbf{B} = B_0 \hat{e}_z$: a low-energy thermal background and an energetic relativistic population. The density ratio between these two populations can be arbitrary. Because our interest is confined to waves with frequencies of the order of the electron cyclotron frequency, which is much greater than the ion plasma frequency, ion dynamics can be neglected. Consequently, the dispersion equation of the linearized Vlasov-Maxwell equations can be written in the form [*Wong et al.*, 1989]

$$\mathbf{D}(\mathbf{k},\omega)=\left(1-\frac{k^2c^2}{\omega^2}\right)\mathbf{I}+\frac{c^2}{\omega^2}\mathbf{kk}+\sum_\alpha \mathbf{Q}^\alpha(\mathbf{k},\omega)=0 \quad \text{(A1)}$$

where

$$\mathbf{Q}^\alpha(\mathbf{k},\omega)=2\pi\frac{\omega_\alpha^2}{\omega^2}\int_{-\infty}^{+\infty}du_\parallel\int_0^\infty du_\perp\frac{u_\parallel}{\gamma}\left(u_\perp\frac{\partial}{\partial u_\parallel}-u_\parallel\frac{\partial}{\partial u_\perp}\right)F_\alpha\hat{e}_z\hat{e}_z$$
$$+2\pi\frac{\omega_\alpha^2}{\omega^2}\int_{-\infty}^{+\infty}du_\parallel\int_0^\infty du_\perp\left[\omega\frac{\partial}{\partial u_\perp}+\frac{k_\parallel}{\gamma}\left(u_\perp\frac{\partial}{\partial u_\parallel}-u_\parallel\frac{\partial}{\partial u_\perp}\right)\right]F_\alpha$$
$$\times\sum_{n=-\infty}^{n=+\infty}\frac{\mathbf{T}^n}{\gamma\omega-n\Omega_e-k_\parallel u_\parallel} \quad \text{(A2)}$$

where $\gamma=(1+u^2/c^2)^{1/2}$, and $\alpha=b,e$ refers to the background and energetic electrons, respectively. The wave vector $\mathbf{k}$ is assumed to lie in the x-z plane so that $\mathbf{k}=k_\perp\hat{e}_x+k_\parallel\hat{e}_z$; $\mathbf{I}$ is the unit dyadic; $\omega_\alpha^2=4\pi n_\alpha e^2/m_\alpha$; $\mathbf{u}$ is the momentum per unit mass and is given by $\mathbf{u}=\mathbf{p}/m_e$; and n_α is the number density of species α. The tensor $\mathbf{T}^n$ is defined by

$$\mathbf{T}^n=\begin{bmatrix}\frac{n^2\Omega_e^2}{k_\perp^2}J_n^2 & -\frac{in\Omega_e}{k_\perp}u_\perp J_nJ_n' & \frac{n\Omega_e}{k_\perp}u_\parallel J_n^2\\ \frac{in\Omega_e}{k_\perp}u_\perp J_nJ_n' & u_\perp^2J_n'^2 & iu_\parallel u_\perp J_nJ_n'\\ \frac{n\Omega_e}{k_\perp}u_\parallel J_n^2 & -iu_\parallel u_\perp J_nJ_n' & u_\parallel^2J_n^2\end{bmatrix} \quad \text{(A3)}$$

where $J_n=J_n(k_\perp u_\perp/\Omega_e)$.

The method for obtaining numerical solutions to the relativistic dispersion equation is cumbersome, and here we only outline the approach employed in reaching the solutions given above. The relativistic factor γ is expanded to $O(u^4/c^4)$, except for the resonant denominator in which we keep the entire expression $\gamma\omega-n\Omega_e-k_\parallel u_\parallel$. One then integrates over $u_\parallel$ analytically and writes the resulting expression in terms of the plasma dispersion function (the Z function defined by *Fried and Conte* [1961]). In contrast to nonrelativistic calculations, the argument of the Z function now depends on $u_\perp$ because of the factor of γ, which appears in the resonance condition. The remaining integration over $u_\perp$ is performed numerically using a standard root-finding algorithm to compute (complex) ω.

Acknowledgments. H.K.W. would like to thank D. Menietti for valuable discussions. This work was supported in part by the Space Physics Theory Program at the Goddard Space Flight Center and NASA grants NAGW-2412 (Neptune Data Analysis Program) and NAGW-1620 to the Southwest Research Institute.

The Editor thanks L.-C. Lee and M. A. Temerin for their assistance in evaluating this paper.

References

Baldwin, D. E., I. B. Bernstein, and M. P. H. Weenink, Kinetic theory of plasma waves in a magnetic field, in *Advances in Plasma Physics*, edited by A. Simon and W. B. Thompson, p. 1, Wiley-Interscience, New York, 1969.

Benson, R. F., M. D. Desch, R. D. Hunsucker, and J. G. Romick, Ground-level detection of low- and medium-frequency auroral emissions, *J. Geophys. Res.*, *93*, 277, 1988.

Chang, T., G. B. Crew, N. Hershkowitz, J. R. Jasperse, J. M. Retterer, and J. D. Winningham, Transverse acceleration of oxygen ions by electromagnetic ion cyclotron resonance with broad band left-hand polarized waves, *Geophys. Res. Lett.*, *13*, 636, 1986.

Crew, G. B., T. Chang, J. M. Retterer, W. K. Peterson, D. A. Gurnett, and R. L. Huff, Ion cyclotron resonance heated conics: Theory and observations, *J. Geophys. Res.*, *95*, 3959, 1990.

Fried, B. D., and S. D. Conte, *The Plasma Dispersion Function*, Academic, San Diego, Calif., 1961.

Gurnett, D. A., W. S. Kurth, I. H. Cairns, and L. J. Granroth, Whistlers in Neptune's magnetosphere: Evidence of atmospheric lightning, *J. Geophys. Res.*, *95*, 20,967, 1990.

Gurnett, D. A., The Earth as a radio source: Terrestrial kilometric radiation, *J. Geophys. Res.*, *79*, 4227, 1974.

Gurnett, D. A., S. D. Shawhan, and R. R. Shaw, Auroral hiss, Z mode radiation, and auroral kilometric radiation in the polar magnetosphere: DE 1 observations, *J. Geophys. Res.*, *88*, 329, 1983.

Hewitt, R. G., D. B. Melrose, and G. A. Dulk, Cyclotron maser emission of auroral Z mode radiation, *J. Geophys. Res.*, *88*, 10,065, 1983.

Kennel, C. F., and M. Ashour-Abdalla, Electrostatic waves and the strong diffusion of magnetospheric electrons, in *Magnetospheric Plasma Physics*, edited by A. Nishida, p. 245, D. Reidel, Hingham, Mass., 1982.

Kurth, W. S., and D. A. Gurnett, Plasma waves in planetary magnetospheres, *J. Geophys. Res.*, *96*, 18,977, 1991.

Lin, C. S., J. L. Burch, S. D. Shawhan, and D. A. Gurnett, Correlation of auroral hiss and upward electron beams near the polar cusp, *J. Geophys. Res.*, *89*, 925, 1984.

Lin, C. S., D. Winske, and R. L. Tokar, Simulation of the electron acoustic instability in the polar cusp, *J. Geophys. Res.*, *90*, 8269, 1985.

Lysak, R. L., Ion acceleration by wave-particles interactions, in *Ion acceleration in the magnetosphere and ionosphere*, *Geophys. Monogr. Ser.*, vol. 38, edited by T. Chang, M. K. Hudson, J. R. Jasperse, R. G. Johnson, P. M. Kintner, M. Schulz and G. B. Crew, p. 261, AGU, Washington, D. C., 1986.

Menietti, J. D., and C. S. Lin, Ray tracing survey of Z mode emissions from source regions in the high-altitude auroral zone, *J. Geophys. Res.*, *91*, 13,559, 1986.

Shawhan, S. D., Magnetospheric plasma waves, in *Solar System Plasma Physics*, edited by C. F. Kennel and E. N. Parker, North-Holland, Amsterdam, 1979.

Temerin, M. A., and D. Cravens, Production of electron conics by stochastic acceleration parallel to the magnetic field, *J. Geophys. Res.*, *95*, 4285, 1990.

Tokar, R. L., and S. P. Gary, Electrostatic hiss and the beam-driven electron acoustic instability in the dayside polar cusp, *Geophys. Res. Lett.*, *11*, 1180, 1984.

Winglee, R. M., J. D. Menietti, and H. K. Wong, Numerical simulations of bursty radio emissions from planetary magnetospheres, *J. Geophys. Res.*, *97*, 17,131, 1992.

Wong, H. K., and M. L. Goldstein, Proton beam generation of whistler waves in the Earth's foreshock, *J. Geophys. Res.*, *92*, 12,419, 1987.

Wong, H. K., and M. L. Goldstein, A mechanism for bursty radio emission in planetary magnetospheres, *Geophys. Res. Lett.*, *17*, 2229, 1990.

Wong, H. K., J. D. Menietti, C. S. Lin, and J. L. Burch, Generation of electron conical distributions by upper hybrid waves in the Earth's solar region, *J. Geophys. Res.*, *93*, 20,025, 1988.

Wong, H. K., D. Krauss-Varban, and C. S. Wu, On the role of the energy of suprathermal electrons in the generation of auroral kilometric radiation, *J. Geophys. Res.*, *94*, 5327, 1989.

Wu, C. S., and L. C. Lee, A theory of terrestrial kilometric radiation, *Astrophys. J.*, *230*, 621, 1979.

Wu, C. S., P. H. Yoon, and H. P. Freund, A theory of electron cyclotron waves generated along auroral field lines observed by ground facilities, *Geophys. Res. Lett.*, *16*, 1461, 1989.

Ziebell, L. F., C. S. Wu, and P. H. Yoon, Kilometric radio waves generated along auroral field lines observed by ground facilities: A theoretical model, *J. Geophys. Res.*, *96*, 1495, 1991.

H. K. Wong, Department of Space Sciences, Southwest Research Institute, San Antonio, TX 78284.

M. L. Goldstein, Laboratory for Extraterrestrial Physics, Code 692, NASA Goddard Space Flight Center, Greenbelt, MD 20771.

(Received May 18, 1993; revised August 9, 1993; accepted August 13, 1993.)

NEPTUNE HIGH-LATITUDE EMISSION AND MAGNETIC MULTIPOLE STRUCTURE

C.B. Sawyer, N.V. King, J.H. Romig, and J.W. Warwick,

Radiophysics, Incorporated, Boulder, Colorado

H.K. Wong

Southwest Research Institute, San Antonio, Texas

N15

Abstract. "High-latitude" radio emission was briefly observed as Voyager approached Neptune's north magnetic pole. The times of maximum emission and of cutoff depend on frequency. Coupled with a magnetic-field model, these data yield information on radio-source location and emission angle. In a dipole field, L-shell and magnetic longitude locate candidate sources of each frequency. Emission angles are then identified with the angle between the modeled magnetic-field direction at the source and the line of sight to Voyager 2 at the times of maximum. At each value of L in the range $6 < L < 9$, there is one source longitude for which emission angle varies smoothly with frequency. The data thus limit source locations to a defined set in the dipole field. Examination of more complex magnetic models [Connerney et al., 1991] shows (1) assumptions of the dipole-based analysis are inconsistent with complex models; (2) the parametric analysis developed here could under some circumstances be extended to a more complex model; (3) the model describes constant-field surfaces with steep slopes that explain qualitatively the observed features of the radio cutoff; and (4) radio emission occurs in association with relatively small-scale magnetic structure described by multipole terms in the magnetic model.

Dipole-Based Analysis

At Neptune the Planetary Radio Astronomy (PRA) experiment observed smooth radio emission in the range 20 to 1326 kHz. Presumably this is extraordinary-mode (X-mode) radiation at the electron cyclotron frequency, $f_c[kHz] = 0.028\ B[nT]$, corresponding to magnetic field B of 714 to 47,357 nT. Radio sources at each frequency lie on a surface of constant field. The magnetometer on Voyager measured fields as strong as 9,695 nT (271 kHz). Voyager must have passed through each source surface with $f_c < 271$ kHz. At each frequency in the range 39.6 to 462.0 kHz reversal of sense of circular polarization accompanied an abrupt drop of intensity. This event was interpreted as X-mode occultation

Dipole radio models in Neptune's multipolar magnetic field

N1S

C. B. Sawyer, N. V. King, J. H. Romig, AND J. W. Warwick,
Radiophysics, Incorporated, Boulder, Colorado

H. K. Wong
Southwest Research Institute, San Antonio, Texas

Abstract. We describe procedures for analyzing data from the Planetary Radio Astronomy experiment. A method to deduce the location and characteristics of the radio sources of Neptune's smooth recurrent radio emission minimizes limiting assumptions and maximizes use of the data, including quantitative measurement of circular polarization. A preliminary broad survey examines all possible source locations at key times. Detailed study of specific sources simulates intensity and apparent polarization of their integrated emission for an extended time period. Time series are modeled here for broad and beamed emission patterns, at two frequencies that exhibit different time variation of polarization. These incomplete results are based on a dipole magnetic model and include only qualitative consideration of polarization transfer. Consideration of a more complex model of Neptune's magnetic field overturns basic assumptions of the dipole-based analysis. Both magnetic polarities occur in both magnetic hemispheres so either sense of polarization can arise in either hemisphere. Irregular elevation of the source surface modifies the radio horizon. Estimating the radio effects, we note evidence of association of sources of Neptune's smooth recurrent emission with magnetic multipolar structure. Multipoles and smooth recurrent emission are simultaneously visible from Voyager; multipolar fields can account for the observed range of radio frequency and for the observed sense of circular polarization.

1. Introduction

With a model of the magnetic field, frequency defines the radial coordinate of a radio source. A cutoff occurs where the index of refraction vanishes: $(f_p/f)^2 + f_c/f = 1$, where f_c is the local value of the electron cyclotron frequency and f_p is the plasma frequency. When $f_p << f_c$, as required by the cyclotron maser theory, the wave propagates at a frequency just above f_c (kHz) = 2800 B (gauss). Radio sources of a given frequency lie on the corresponding constant-field surface defined by the magnetic model.

The Planetary Radio Astronomy (PRA) experiment measured the time variation of intensity and circular polarization over a range of radio frequencies at Neptune [*Warwick et al.*, 1989]. PRA's incomplete set of measurements precludes direct determination of source direction and polarization at a given moment. PRA experimenters have devised a number of ways, listed below, to locate sources and estimate the emission angle using the existing data.

Source location basically assumes extraordinary-mode (X-mode) emission and matches magnetic-field direction to the observed sense of circular polarization. Planetary radio sources have traditionally been located in the appropriate auroral zone, with emission in a hollow cone at wide angle to the local magnetic (dipole) field. Another basic technique identifies the beginning and end of a period of emission with source passage across the radio horizon, the limit of visibility of X-mode emission [*Desch and Kaiser*, 1987]. A third method depends on the fact that circular polarization detected by the PRA instrument vanishes when the source is on the antenna electric plane [*Warwick et al.*, 1977]; a spacecraft maneuver